

Old Dominion University

ODU Digital Commons

Electrical & Computer Engineering Theses &
Dissertations

Electrical & Computer Engineering

Spring 2018

A Dual Resonant Transformer and a Dielectric Antenna for Picosecond Pulse Radiation

Khiem Huynh

Old Dominion University, khuyn006@odu.edu

Follow this and additional works at: https://digitalcommons.odu.edu/ece_etds



Part of the [Electrical and Computer Engineering Commons](#)

Recommended Citation

Huynh, Khiem. "A Dual Resonant Transformer and a Dielectric Antenna for Picosecond Pulse Radiation" (2018). Master of Science (MS), Thesis, Electrical & Computer Engineering, Old Dominion University, DOI: 10.25777/rtep-er12

https://digitalcommons.odu.edu/ece_etds/34

This Thesis is brought to you for free and open access by the Electrical & Computer Engineering at ODU Digital Commons. It has been accepted for inclusion in Electrical & Computer Engineering Theses & Dissertations by an authorized administrator of ODU Digital Commons. For more information, please contact digitalcommons@odu.edu.

**A DUAL RESONANT TRANSFORMER AND A DIELECTRIC ANTENNA FOR
PICOSECOND PULSE RADIATION**

by

Khiem Huynh
B.S. December 2016, Old Dominion University

A Thesis Submitted to the Faculty of
Old Dominion University in Partial Fulfillment of the
Requirements for the Degree of

Master of Science

Electrical and Computer Engineering Department

OLD DOMINION UNIVERSITY
April 2018

Approved by:

Shu Xiao (Advisor)

Shirkshak Dhali (Member)

Yucheng Zhang (Member)

ABSTRACT

A Dual Resonant Transformer and a Dielectric Antenna for Picosecond Pulse Radiation

Khiem Huynh
Old Dominion University, 2018
Director: Shu Xiao

This thesis discusses the development of a pulsed power system for high power picosecond pulse radiation. In the system, a charging transformer, which generates a high voltage pulse of ~ 100 kV, can be used for charging a transmission line in less than 100 ns. Such a short pulse could cause a peak gap switch to break down and generate a picosecond pulse transient for radiation. A dielectric antenna, if fed with the high voltage picosecond pulses, can radiate them to targets made of high dielectric materials. Biological tissues, for instance, can be targeted for electrostimulation.

The transformer was designed considering the needs to deliver a high gain and fast output. We showed that a transformer in the dual resonant mode, in which the resonance of the primary and the secondary is equal, can produce a voltage gain of approximately 6. The output voltage of the transformer is more than 100kV with an input of 15kV. This shows the average gain of the transformer is 7. The fast output requires the voltage at the secondary winding needs to be less than 100 ns in order for achieving a picosecond transient in the oil peak switch. This was done by low-inductance windings with an air core. Two winding configurations were explored: a cylindrical winding and a toroidal winding. The cylindrical winding appears to be a better option in terms of the gain. Experimental results show that for a capacitive load (30pF), the voltage can be charged up to 33 kV in 20 ns.

A conical dielectric antenna was investigated through simulation and experiments. The antenna is made of a V-shape transmission line on a ceramic conical body with dielectric constant of 28. This antenna was immersed in transformer oil for high voltage insulation, which allowed for the feed voltage to be as high as 50 kV. The antenna was characterized by an electric field sensor immersed in water. We found that the emitted field increases as the voltage increases, but it reaches a saturation for 40 kV. The highest electric field is 1.5 kV/cm even for the input voltage 50 kV. This is 6 times less than simulation. We speculate that the discrepancy is caused by the dielectric tangent loss, which was not taken into account in the simulation.

Future work towards a complete system includes a choice of a linear dielectric material which is capable of sustaining its dielectric constant for a high electric field and the study of an oil peak switch, which is a critical component between the transformer and the antenna.

Copyright, 2018, by Khiem Huynh, All Rights Reserved.

This thesis is dedicated to my wonderful family.

ACKNOWLEDGMENTS

First, I would like to give my deepest and finest appreciation to my advisor, Dr. Shu Xiao, for being such a wonderful advisor. I am grateful to have Dr. Xiao as my advisor, his guidance and support are countless. He consistently allowed this paper to be my own work and directed me in the right direction whenever he thought I needed it.

I would also like to thank Dr. Shirshak Dhali and Dr. Yucheng Zhang for their time and interest in serving as committee members for my thesis. I am thankful for their comments and feedback. I am also grateful to Dr. Chunsheng Xin, Graduate Program Director of the Electrical and Computer Engineering Department, for his advice and support. Last but not least, I would like to thank my fellow graduate student, Ross Petrella, and visiting professor, Prof. Xianbing Zou for their help.

Lastly, I would like to thank my family for their unconditional love and support. For my mom, my dad, my brothers, Mr. Trung Nguyen, Mrs. Anh Dang, and my girlfriend Ms Chau Nguyen who have been such a wonderful source of inspiration and encouragement. Thank you.

NOMENCLATURE

| | |
|----------------|------------------------------------|
| <i>C</i> | Capacitor |
| <i>DiBiCa</i> | Dielectric Bipolar Conical Antenna |
| <i>DRPT</i> | Dual Resonant Pulse Transformer |
| <i>EM</i> | Electromagnetic |
| <i>EMP</i> | Electromagnetic pulses |
| <i>E-field</i> | Electric field |
| <i>H-field</i> | Magnetic field |
| <i>IRA</i> | Impulse Radiating Antenna |
| <i>k</i> | Coupling coefficient |
| <i>L</i> | Inductor |
| <i>M</i> | Mutual inductance |
| <i>PEC</i> | Perfect electric conductor |
| <i>R</i> | Resistor |

TABLE OF CONTENTS

| | Page |
|--|------|
| LIST OF TABLES | ix |
| LIST OF FIGURES | x |
| Chapter | |
| Chapter 1. Introduction | 1 |
| 1.1 A High Power Ultrashort System | 1 |
| 1.2 Transformer basics | 3 |
| 1.3 Picosecond Pulse Antennas | 6 |
| Low power antennas | 7 |
| High power antennas | 11 |
| 1.4 Objectives of This Thesis | 14 |
| 1.5 Outlines | 15 |
| Chapter 2. Dielectric Biconical Antenna | 16 |
| 2.1 Antenna Configuration | 16 |
| 2.2 Construction of Antenna | 20 |
| 2.3 Feed Structure | 23 |
| 2.4 3D Simulations | 26 |
| 2.5 Experimental Setup | 35 |
| 2.6 Experimental Results | 39 |
| 2.7 Summary | 44 |
| Chapter 3. A Pulse Transformer | 45 |
| 3.1 A DRPT | 46 |
| 3.2 Construction of transformer - Design 1: Helical Configuration | 49 |
| 3.3 Multisim simulation | 51 |
| 3.4 Experimental Setup | 53 |
| 3.5 Experimental Results | 56 |
| 3.6 Design 2: Toroidal Transformer | 58 |
| 3.7 Summary | 62 |
| Chapter 4. Discussions | 63 |
| Future work | 66 |
| Chapter 5. Summary | 67 |
| REFERENCES | 68 |
| APPENDICES | 75 |
| VITA | 80 |

LIST OF TABLES

| Table | Page |
|--|------|
| 1: Design approach differences..... | 22 |
| 2: 3D Simulation Results at different distance | 27 |
| 3: Low voltage experimental results at different input voltages with various distances | 40 |
| 4: High voltage experimental results at different input voltages (30-50 kV) with various distance (2-20mm) | 41 |
| 5: A comparison of simulation and experimental results with different input voltage..... | 44 |
| 6: Transformer Design Parameters | 50 |
| 7: Gain vs. coupling coefficient of a helical transformer..... | 52 |
| 8: Measured secondary voltages for given primary voltages..... | 56 |
| 9: Toroidal transformer values..... | 60 |
| 10: A comparison of leakage inductances effects on transformer gain. | 64 |

LIST OF FIGURES

| Figure | Page |
|---|------|
| 1: A block schematic diagram of an EMP system | 1 |
| 2: Leakage inductance and magnetizing inductance of a practical transformer [10] | 4 |
| 3: A basic circuit of a practical transformer.[10] | 6 |
| 4: A patch antenna with descriptions [12] | 7 |
| 5: A horn antenna design with description [14]..... | 9 |
| 6: a) Exponential tapered (Vivaldi) b) Linearly tapered c) Constant width slot antenna.[16]..... | 10 |
| 7: Reflector and Lens IRA with description [20]..... | 11 |
| 8: Basic traveling wave element for electromagnetic field evaluation [29] | 12 |
| 9: Antenna design (an exploded view)..... | 16 |
| 10: An assembled view | 17 |
| 11: Azimuth angle of the PEC cone [28]..... | 19 |
| 12: Characteristic impedance of the PEC cone..... | 19 |
| 13: Antenna design with dimension..... | 20 |
| 14: Copper paint deposition technique | 21 |
| 15: Constructed antenna model with resistor ring | 23 |
| 16: Parallel plates feed structure | 24 |
| 17: Coaxial cable breakout [30]..... | 24 |
| 18: Constructed parallel feed structure | 25 |
| 19: Antenna 3D simulation model | 26 |
| 20: Electric Field Simulation in water and oil | 27 |
| 21: 3D Simulation (E-field) in oil..... | 29 |
| 22: E-field Direction in oil..... | 30 |
| 23: H- field Simulation in oil..... | 31 |
| 24: Current distribution of the PEC triangular PEC cone..... | 32 |
| 25: Current flow after the wave is radiated..... | 33 |
| 26: a) Antenna 3D model. b) E-field simulation at 1.2 ns..... | 34 |
| 27: Produced electric field at specific time and its focal point..... | 34 |
| 28: a) Produced E-field with and without the resistor ring. b) Produced E-field of various conductance values. | 35 |
| 29: a) Schematic for experimental setup for voltage testing b) Experimental picture for low voltage testing. | 36 |
| 30: Antenna structure with a bottle housing | 37 |
| 31: a) Schematic for experimental setup for high voltage testing b) Experimental picture for high voltage testing | 38 |
| 32: Antenna waveform at 10mm gap distance and 10kV input voltage is applied..... | 39 |
| 34: Low voltage trend line at different testing input voltages | 40 |
| 35: High voltage trend line at different testing input voltages..... | 42 |
| 36: Experimental results trend line at 5, 10 and 20 mm | 43 |
| 37: Block diagram and circuit diagram of a DRPT | 45 |
| 38: a) First swing charging cycle. b) Dual resonant charging cycle. [35] | 46 |
| 39: Helical wire/strip transformer [35] | 47 |
| 40: A DRPT equivalent circuit [35]..... | 48 |

| | |
|--|----|
| 41: Multisim model of a helical transformer | 51 |
| 42: Transient of ideal coupling coefficient on a helical transformer | 52 |
| 43: First experiment schematic and setup | 53 |
| 44: Second experiment schematic and setup | 55 |
| 45: Transformer gain decay rate compares to linear trend line | 57 |
| 46: Helical transformer output transient | 58 |
| 47: Reed relay triggered results along with input and output voltage of a helical transformer | 58 |
| 48: Toroidal DRPT design with label | 59 |
| 49: Toroidal DRPT simulation schematic..... | 60 |
| 50: Simulated toroidal transformer result | 61 |
| 51: a) Toroidal DRPT output transient without peaking switch b) Toroidal DRPT output transient with peaking..... | 61 |
| 52: Decay rate of transformer as the leakage inductance increases compares to linear decay trend line..... | 65 |
| 53: Transient of transformer with various leakage inductance values..... | 66 |
| 54: Peaking switch with parallel plate transmission line integration..... | 75 |
| 55: A combination Pockels cells with polarizer for Electric field sensing..... | 76 |
| 56: eoProbes setup for electric field measurements..... | 77 |

Chapter 1. Introduction

1.1 A High Power Ultrashort System

High power ultrashort pulse radiation, also known as electromagnetic pulse (EMP), refers to a transient electromagnetic disturbance [1-6]. The radiation, which is dependent on the source and radiator, can be either electric or magnetic. In general, an EMP system consists of several sections of pulsed power systems (Figure 1). Prior to the transformer section is the low voltage, high energy power supply, which is usually a series of capacitors, charged by a DC power supply. The transformer section allows the low voltage determined by the previous section to step up to a much higher voltage. This section sometimes can be replaced by a different high voltage converter such as a Marx generator to meet the experimental conditions. The transfer section allows to store the high voltage pulse after the transformer, but this pulse can be reduced in pulse length through a peaking section. An ultrafast peaking switch breaks down upon the reduced pulse duration and causes a very fast transient, which is useful for antenna radiation. There were many EMP systems built in the past. For example, an EMP system was reported to produce a pulsed electric field [6] with a rise time of 1ns. In another system, the combination of a Tesla transformer and a Marx generator that synchronizes the peaking stage and crowbar switch is capable of generating electric field with 300 ps rise time with a magnitude of 450 kV and a help of a Valentine travelling wave antenna. [6]

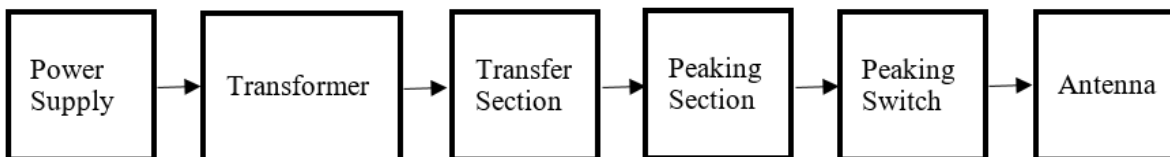


Figure 1: A block schematic diagram of an EMP system

At the Center for Bioelectrics, Old Dominion University, an EMP was developed to generate ultrashort and intense electric pulses for biological applications. Subnanosecond pulses were radiated through a dielectric rod antenna. The output of the electric pulse was approximately 500 ps and the magnitude was 0.6kV/cm [2]. This value is far less than the required electric field (20kV/cm) at which significant biological response, for example, cell permeabilization, can be induced [11]. Besides the low intensity pulse radiation, the system itself is bulky and occupies a large space, which makes it impossible to move freely for the use of exploring other biological processes that may require much weaker electric fields.

In this thesis, effort has been made to develop a compact EMP system. It has the same structure as that shown in Figure 1. Specifically, a compact transformer that is capable of operating at 100 kV was developed. A compact dielectric antenna was studied through simulation. It was characterized in both frequency domain and time domain. Due to the time limitation, they were studied separately and were not tested as a whole system. The highest testing voltage for the antenna was 50 kV generated by a commercially available pulse source.

1.2 Transformer basics

A transformer transfers energy from one circuit to another without being electrically connected. The process can be understood from Faraday's induction Law. A typical transformer is consisted of two windings wound around the transformer core. The transformer core is usually made of magnetic material that has a high permeability which helps to confine and guide the magnetic flux that generates from the transformer circuit.

According to Faraday's Law, once a varying or an alternating current is applied to the transformer primary winding, a varying magnetic flux is produced within the core of the transformer. Since both the primary and secondary are wound to the same core, the varying magnetic flux is also seen in the secondary winding. The changing flux causes induction of electromotive force and current flow when a load is connected across the secondary stage. In an ideal transformer, the voltage of the primary is directly related to the number of turn on the secondary pair with the change in magnetic flux: [7-10]

$$V_s N_s = - \frac{d\phi}{dt} \quad (1)$$

$$V_p N_p = - \frac{d\phi}{dt} \quad (2)$$

Where,

V_p is the primary voltage

V_s is the secondary voltage

N_p is the number of turn on the primary

N_s is the number of turn on the secondary

Φ is the magnetic flux

From the above equations, the turn ratio is the only parameter that determines the characteristic of the transformer. The primary and secondary voltages are related by the following:

$$V_p N_s = V_s N_p \quad (3)$$

Eq.3 implies the coupling coefficient in an ideal transformer is 1 and all the energy will be transferred. Unfortunately, a practical transformer will have a lower coupling coefficient due to leakage fluxes. As a result, the voltage transfer ratio will not only be governed by the turn ratio. Furthermore, the energy transfer is accompanied by the core's Joule heating due to eddy current or hysteresis loss.[7-10]

In general, the flux that is lost in both the primary and secondary windings can be expressed as leakage inductances. The common flux that links the primary winding and secondary winding is the effective part that causes a voltage transformation.

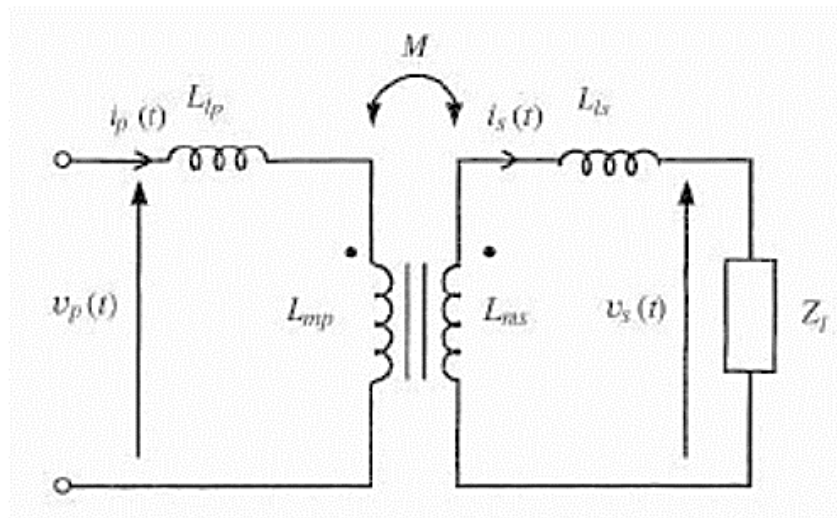


Figure 2: Leakage inductance and magnetizing inductance of a practical transformer [10]

In the transformer equivalent circuit, L_{lp} is the primary leakage inductance and L_{sp} is the secondary leakage inductance. L_{mp} and L_{ms} are the magnetizing inductance for both

primary and secondary stage. Considering the coupling coefficient, a voltage equation is obtained using the Kirchhoff's Voltage Law.

$$V_p(s) = s[L_p I_p(s) - M I_s(s)] \quad (4)$$

Where,

$$L_p = L_{lp} + L_{mp} \quad (5)$$

$$L_s = L_{ls} + L_{mp} n^2 \quad (6)$$

$$M = n L_{mp} \quad (7)$$

$$k = \frac{M}{\sqrt{L_s L_p}} \quad (8)$$

Note that k is the coupling coefficient, M is the mutual inductance, and n is the number of turn on the secondary.

A complete equivalent circuit of a practical transformer should also consider the wire resistance of the windings, core's equivalent resistor, representing eddy current loss, and hysteresis loss. Next, the electric coupling between the primary and secondary windings is reflected in the capacitance Cps. (See Figure 3). These values are very important in designing the transformer process, especially the leakage inductances. This can be directly related to the gain of the transformer. The larger the leakage inductances the smaller the gain. These basic parameters are fundamental in constructing a design of a transformer.

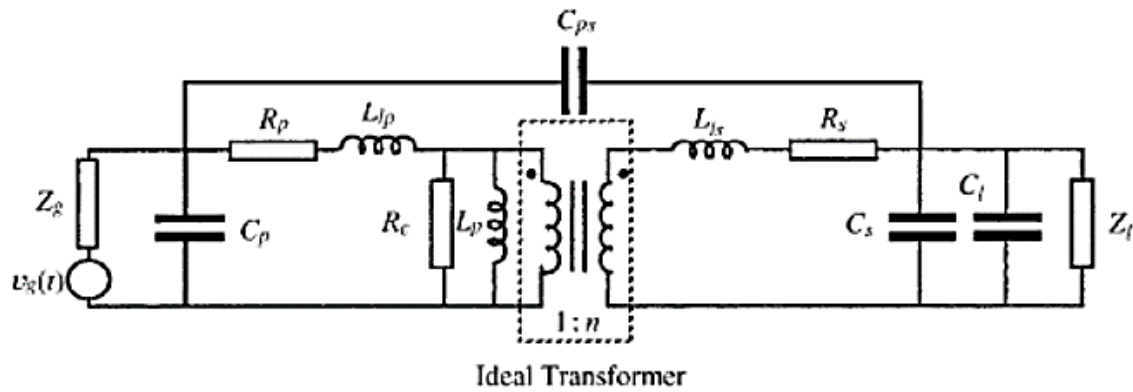


Figure 3: A basic circuit of a practical transformer.[10]

1.3 Picosecond Pulse Antennas

In the EMP system, the radiated pulses are usually in the nanosecond or subnanosecond range. Such pulses contain a broad spectrum, which covers from hundreds of megahertz to several gigahertz. Broadband antennas are used to radiate the pulses. Preferably, a frequency-independent antenna should be the prime option. Generally speaking, there are two types of antennas that can be qualified as frequency-independent antennas: 1) a travelling wave antenna, which provides a wave-guiding structure that allows a transverse electromagnetic (TEM) wave to propagate and emit; and 2) a resonant antenna with multiple resonant frequencies. Near each resonant frequency, there is a finite bandwidth for which the antenna works as a narrowband radiator, but the overall bandwidth is expanded when several resonant frequencies are considered all together. For a subnanosecond or a nanosecond pulse, both travelling wave antenna and resonant antenna can be used. In the context of a high power EMP, these antennas must be designed to withstand high voltage pulses in order to avoid dielectric breakdown or surface flashover.

Low power antennas

For low power antenna, there are several designs that can be readily adopted including a patch antenna, a TEM horn, and a Vivaldi antenna. A patch antenna is also known as a microstrip antenna and it is a resonant antenna. It has a two-dimensional geometry (see Figure 4). This type of antenna is constructed with a base of an insulating dielectric substrate. A metal patch with a desired shape are covered on the dielectric substrate to work at various frequencies, which can go as high as 100 GHz. Special details can be given on the cornering, distance and width of the patch, which can lead to different resonant frequencies. Also, a microstrip antenna can be designed to produce various polarizations [12-13]. Since a patch antenna consists of a radiating patch on a dielectric substrate and a ground plane on the other side of the substrate, the radiation usually happens between the edge of the patch and the ground plane.

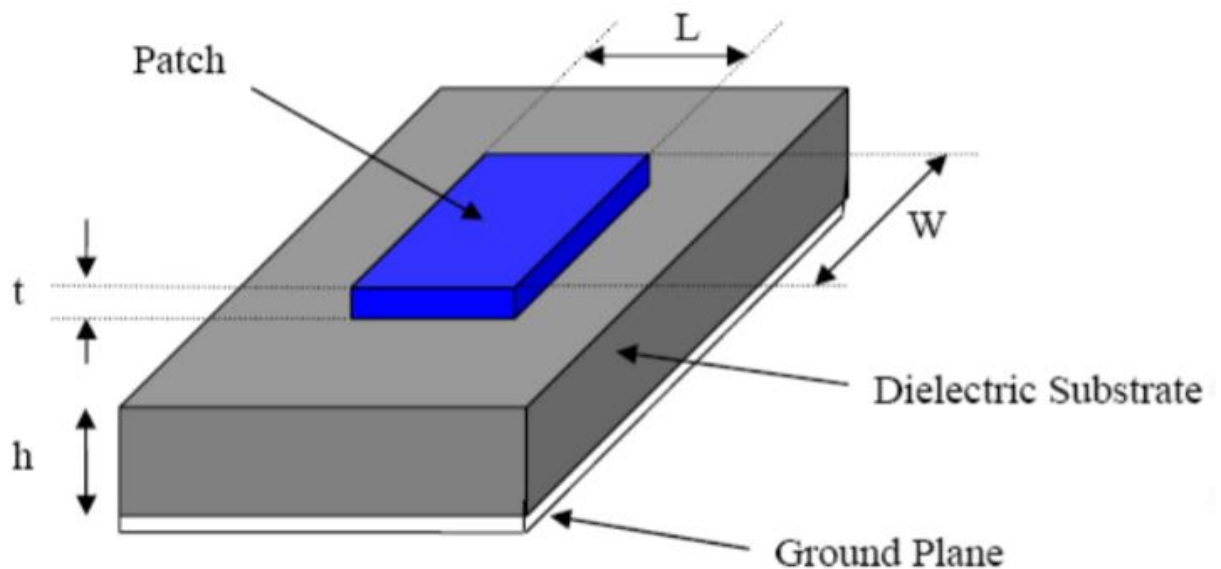


Figure 4: A patch antenna with descriptions [12]

The length L of the patch is considerably smaller than $\frac{\lambda}{2}$ of the fundamental TM_{10} mode excitation, where λ is the wavelength in the dielectric medium. In order to increase the field from the patch antenna, the dimension of the patch should be increased, as well as increasing the substrate thickness or decrease the dielectric constant of the substrate. Because this type of antenna can be made compact in a 2-D structure, it is suitable in mobile communication or global positioning system. Their limitations are narrow bandwidth, low gain, low efficiency, and great ohmic loss in feed structure. The narrow bandwidth however can be overcome by designing patches that allow for the existence of multiple TM modes.

A TEM horn antenna is a travelling wave antenna and frequently used in wideband applications, such as in Ground Penetrating Radar or biomedical imaging. It is capable of radiating an impulse with very little distortion. Dielectric loading can be applied to reduce the size of this antenna. A typical horn antenna consists of a metal waveguide that attaches to a flared horn to direct the signal. The structure of this antenna helps to transition from the impedance of the waveguide to free space. If the presence of the flared or tapered out section does not exist, the sudden transition will occur and cause the signal to reflect back to the waveguide as standing waves. Figure 5 shows below an example of a typical horn antenna [13-14]. A modified version of this antenna has a transition from the center of a coaxial cable into two resistive launch planes. This resistance suppresses the reflection of the launching plate. [13-14]

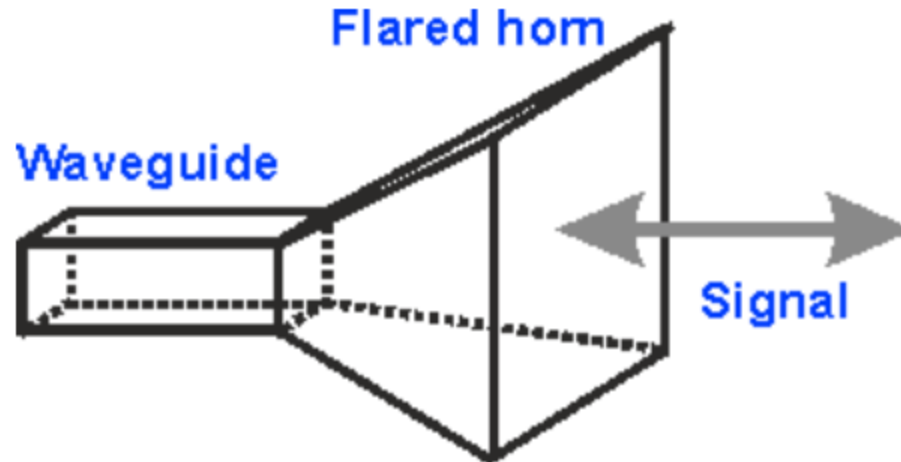


Figure 5: A horn antenna design with description [14]

The horn antenna dimension is directly related to its performance. As the size of the horn antenna increases, the bandwidth becomes broader. The advantage of a horn antenna is it provides a simple interface to a waveguide. On the other hand, a horn antenna limits itself from various applications that require compactness and mobilization.

Another candidate for broadband application is the Vivaldi antenna. It is a tapered slot antenna, which can be constructed by attaching metal sheets on one or both side of a dielectric plate. The tapered slot section of such an antenna assists guiding the wave from the feed and radiates it to free space [15-16]. There are several types of Vivaldi antennas, including those that are exponentially tapered, linearly tapered, and constant-width (Figure 6).

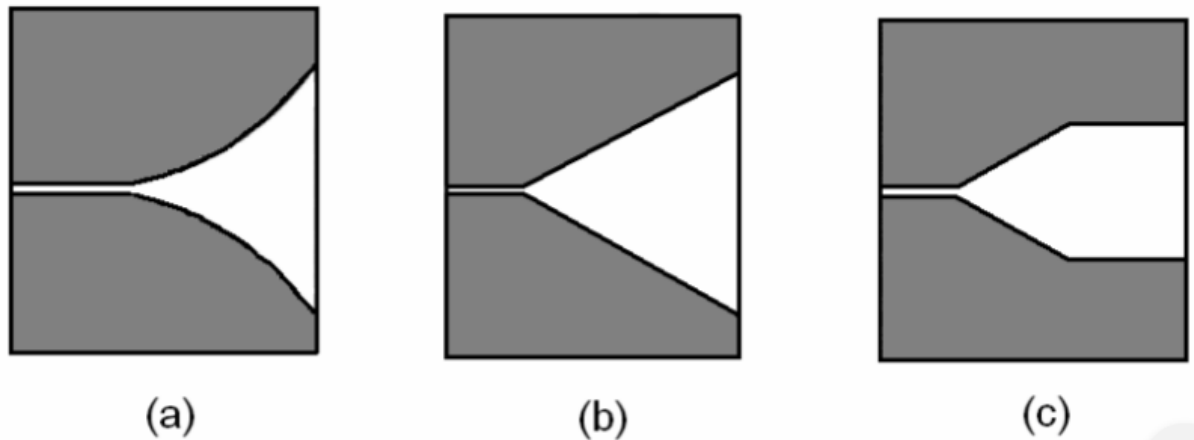


Figure 6: a) Exponential tapered (Vivaldi) b) Linearly tapered c) Constant width slot antenna.[16]

Vivaldi antenna is classified as a surface travelling wave antenna. In the design of such antenna, the separation between two plates is also smaller than $\frac{\lambda}{2}$. The wave that travels along the antenna is bound between the two conductors of the antenna. The dielectric substrate is important to the antenna performance, which is to narrow the main beam of the antenna. Increasing the thickness of the substrate increases the gain of the antenna. A low dielectric constant material should be considered for the dielectric substrate. A high dielectric substrate can cause some scattering effects of the surface travelling wave. [15-16]

High power antennas

An Impulse radiating antenna, as known as IRA, has been widely studied as wideband EMP antenna. There are two typical IRAs, which are reflector IRA and lens IRA (Figure 7). The reflector IRA has a paraboloidal reflector fed by a conical TEM structure, which has an impedance to conserve a cardioid pattern at low frequency [17-26]. The lens IRA is a simple TEM horn antenna feeding a dielectric lens. It is meant for focusing and confining waves.

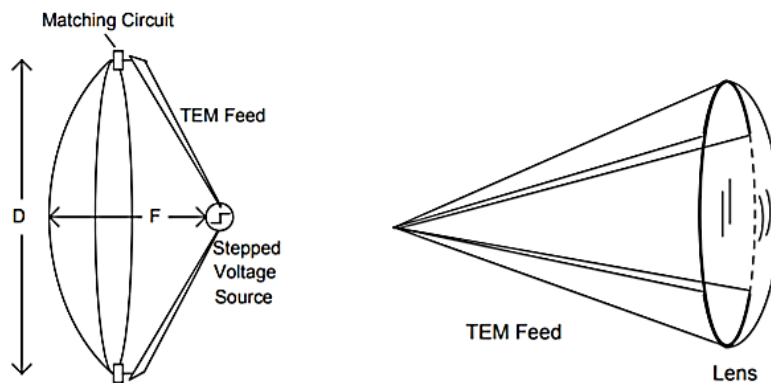


Figure 7: Reflector and Lens IRA with description [20]

The pulse radiated from a reflector IRA has three phases, a prepulse, an impulse, and a tail. A spherical wave emits from the first focal point of the reflector. It either travels backward and toward the reflector or forward and away from the reflector. The backward part is reflected by the reflector and converges at the second focal point, forming the impulse that has the largest magnitude. The forward part arrives at the second focal point earlier but has a lower magnitude due to the divergence. The impulse has an opposite polarity to the prepulse. The tail pulse is caused by the diffractions at the reflector aperture [26].

A lens antenna produces a simpler waveform. It only has an impulse and a tail pulse. The impulse originates from the TEM transmission line and is the wave after passing the lens. An impedance matching network is usually placed at the end of the TEM line and can absorb most of the low frequency components of the feed signal. But some high frequency components can escape and cause the tail pulse.

Radiation from a travelling antenna

Electromagnetic radiation is the results of the speed change of moving charges. A traveling wave element, which is a wire antenna with a termination, can be used to understand the radiated electromagnetic field. [29]

In Figure 8, the axis of a wire antenna is aligned with the x axis. Once a traveling wave from the source is generated, it will propagate along the antenna with the speed of light c until it reaches the termination. [29]

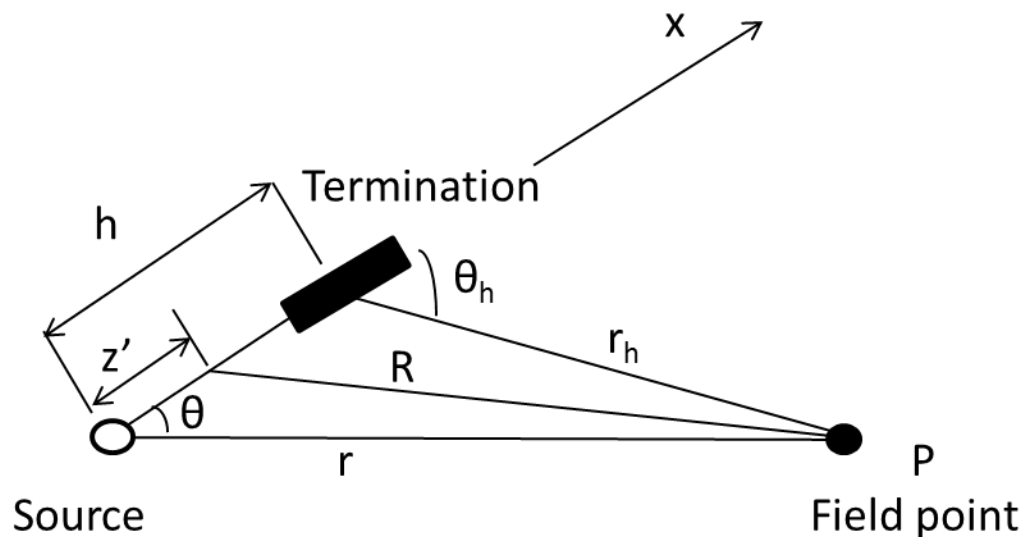


Figure 8: Basic traveling wave element for electromagnetic field evaluation [29]

During the wave propagation, negative charges, q_o , stay at the source, and positive charges, q_h , leave the source. The resulting electric field of this current source (I_s) is a function of time, which have r and θ at the origin of the source. In the limit as $r \rightarrow \infty$, the electric field (far zone field) at that point only has θ component:

$$E^r = \frac{\mu_0 \sin \theta}{4\pi r(1 - \cos \theta)} c I_s \left\{ \left(t - \frac{r}{c} \right) - \left[t - \frac{r}{c} - \frac{h}{c} (1 - \cos \theta) \right] \right\} \hat{\theta} \quad (12)$$

Where, $I_s(t)$ is the current source that can be a Gaussian pulse and $I_s(t) = I_o e^{-\left(\frac{t}{\tau}\right)^2}$ (13)

The electric field in principle consists of two radiation terms: the first that originates from the source with a delay of $\frac{r}{c}$; and the second originates from the termination with a delay $\frac{r}{c} + \frac{h}{c} (1 - \cos \theta)$. These radiations coincide with the two locations where the change of charge speed takes place. As far as the field from the charge themselves (Coulomb field), it decays much faster with a $\frac{1}{r^2}$ dependence.

1.4 Objectives of This Thesis

The purpose of the work of this thesis was to create a compact, portable EMP system which has the capability of radiating an intense and ultrafast electric field. The work includes the development of a dual resonant transformer for fast charging and an impulse radiating antenna for picosecond pulses.

A dual resonant transformer is in charge of creating ultrafast and high voltage pulses, which will not be directly radiated by the antenna. Rather, it serves as a charging pulse to the peaking stage and peaking switch, which are responsible of producing fast-transient pulse. The integration of the transformer and a peaking switch helps to reduce the submicrosecond charging pulse to subnanosecond radiating pulses.

An impulse radiating antenna was developed based off a dielectric lens IRA concept. It has a V-shaped, metal TEM wave structure, wrapped on a dielectric cone. The wave launched from this conical structure converges at a secondary dielectric cone before impinging upon the tissue. We termed this antenna as dielectric biconical antenna (DiBiCA). It was designed to interface between the transformer-based pulsed charging system and a biological tissue that has a high dielectric constant. So the antenna dielectric constant can be chosen to be close to the tissue property, allowing for a maximal power transmission.

The produced electric field in the tissue can potentially stimulate biological responses for biomedical applications.

1.5 Outlines

In Chapter 2, the description of the DiBiCA is provided. Next, a 3D electromagnetic simulation was performed to design the antenna. The construction of such antenna is also presented. Furthermore, experiments were performed to validate the antenna design.

In Chapter 3, the theory of the dual resonant air core transformer is discussed. A Multisim model of the circuit was built to simulate the transformer characteristic. Next, the transformer was constructed and tested.

In Chapter 4, discussion is presented for future improvements and Chapter 5 will conclude this thesis.

Chapter 2. Dielectric Biconical Antenna

A dielectric biconical antenna (DiBiCA) resembles a lens in that they both establish a travelling wave in a dielectric. The energy is confined in the dielectric before emitting to the free space. DiBiCA is simpler and does not require a wave front of the same phase as required for a lens antenna to focus.

2.1 Antenna Configuration

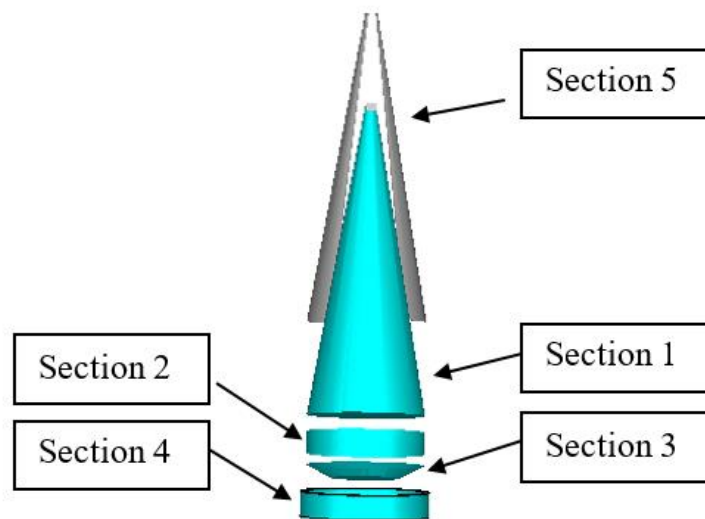


Figure 9: Antenna design (an exploded view)

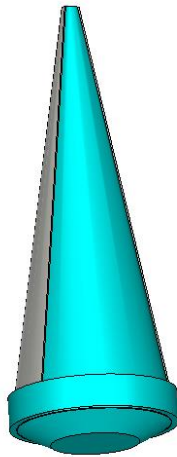


Figure 10: An assembled view

The antenna consists of five different sections. Section 1 is the wave launching section. Section 2 is the dielectric waveguide. Section 3 is the wave emitting section. Section 4 is the resistor ring. Section 5 is the V-shape antenna. Figure 9 shows the full picture of each section separately using the translate function in CST studio. Each section of the antenna has its own purpose.

Section 1 and 5 are responsible for launching waves. Section 5 consists of two triangular conductive plates that are bent in a conical shape to cover section 1. If the plates are infinite, the antenna is a travelling antenna and has a wide bandwidth. But the truncation of the antenna to a finite length made this antenna act like a small aperture antenna and thus it has a finite bandwidth.

Section 2 is a dielectric rod. The electromagnetic waves travel from the wave launching section and will be confined and guided to the next section, the emitting section. A hybrid wave that has transverse electric and magnetic components is established in this section.

Section 3 radiate the electric field into either a free space or a target. The conical shape of this section makes it acts like a convex lens which confine the electric field to a small area. The target can then have a good spatial resolution. Section 4 is the resistor ring. It is added to the

end of Section 5 to eliminate some low-frequency waves bouncing back. The material of the resistor is conductive PLA. The resistor ring was modeled using CST studio software and created using a Dremmel 3D printer. The ring was press-fit to Section 3, the wave emitter section, so the ring connects both conductive plates (Section 5).

This antenna was designed to target skin, so the material dielectric constant should be close to that of a skin (40). After a research of the available materials, we chose DURA-Z™ (TTZ), which is a composite material of MgO and stabilized zirconia. According to the datasheet from the manufacturer, the dielectric constant of this material is 28. Knowing the dielectric constant allows us to determine the radius of the antenna rod for a given pulse duration: [28]

$$\sqrt{\varepsilon_r}R > t_p c_0 \quad (9)$$

Where,

t_p is the pulse duration

c_0 is the speed of light

ε_r is the relative permittivity

R is the antenna rod radius

This condition means that laterally the boundary from the rod to the air shouldn't cause a strong reflection for most of the pulse.

The characteristic impedance of the wave launching section, mainly for Section 5, can be calculated using the following equation [28]:

$$2Z_o = \frac{Z_c}{\sqrt{\varepsilon_r}} \frac{k(\cos \phi_0)}{k(\sin \phi_0)} \quad (10)$$

Where,

$$k = \int_0^{\frac{\pi}{2}} \frac{d\beta}{\sqrt{1-m(\sin \beta)^2}} \quad (11)$$

From this equation, m is a result of the function $\cos \phi_0$ and $\sin \phi_0$, where $0 < \phi_0 < \frac{\pi}{2}$. Z_c is the free space impedance which is equaled to 377 ohms and ϵ_r is the dielectric permittivity of the dielectric material. In case the dielectric constant of TTZ, which is 28. From the equation above, we can map the azimuth angle (ϕ_0), which is correlated to the spread of the PEC (perfect electric conductor) cone of Section 5. The angle ϕ_0 is calculated using an elliptic integral function provided by Matlab. The following graphs show the description of ϕ_0 and the character impedances of this TTZ antenna.

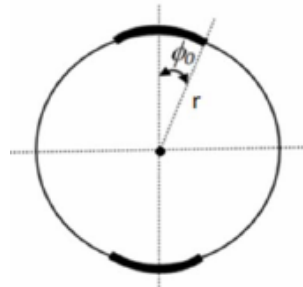


Figure 11: Azimuth angle of the PEC cone [28]

Characteristic Impedance

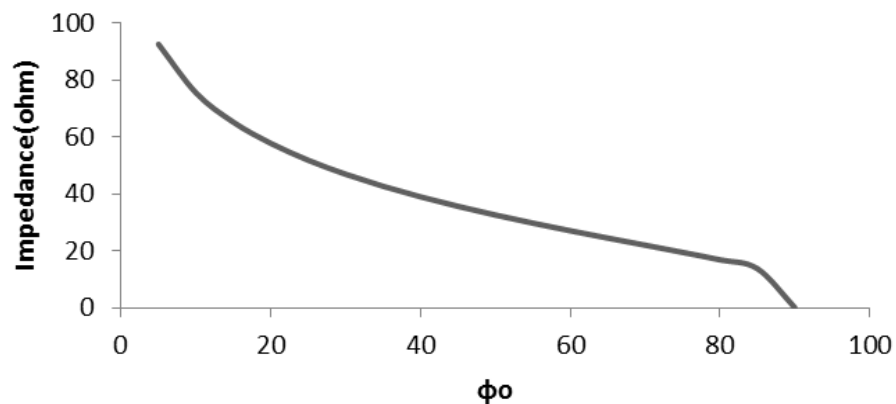


Figure 12: Characteristic impedance of the PEC cone

The characteristic impedance is tightly related to the azimuth angle, which varies from 0 to 90°. As the angle increases the impedance decreases. The impedance is infinite when ϕ_0 is zero and approaching zero when ϕ_0 is 90° (short circuit). However, the desired characteristic impedance is 50Ω, which makes ϕ_0 to be 26.75°.

In general, this design is a modified version of a previous antenna that has a low dielectric constant [2]. However, this antenna has a longer wave launching section ($l\sqrt{\epsilon_r}$) than the original design, which has the advantages in frequency independence, uniform azimuthal directivity, and TEM mode excitation [28]. In addition, the dielectric waveguide section is shorter, which may reduce dielectric loss and broadening effects of the pulses travelling back from the wave launching section. One last difference of this design is that the tip of the wave emitting section is flat in order to reduce the leakage loss to the free space.

2.2 Construction of Antenna

The construction of this antenna requires several techniques. First of all, the antenna body was machined by using a diamond tip tool to grind the TTZ material into a desired conical shape. The dimension of the antenna is shown below (Figure 13).

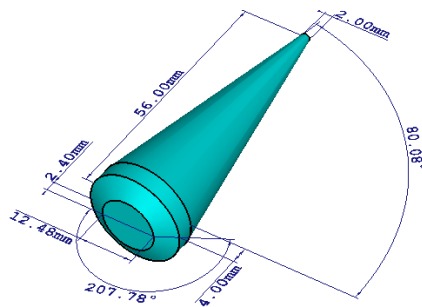


Figure 13: Antenna design with dimension

After the antenna dielectric body was created, the PEC cone section was the next concern. Several options were considered to ensure the PEC-dielectric material to have a smooth and tight contact. The two triangular conductive plates were first made from a copper tape. This material is fairly cheap. It has one smooth surface and an adhesive is on the other side. It is very easy to attach to any surface including the TTZ material. However, after the plates were pressed to attach the antenna body, they cannot stay long. Since the antenna was immersed in different liquids like water or oil, the adhesion become loose. Therefore, we had to replace the copper plates from time to time. But within a couple days, the copper plate seemed pretty stable on the antenna dielectric body.

Besides the copper tape, another approach was using conductive copper paint. The conductive copper paint contains tiny copper particles. Two triangular conductive plates were created by depositing multiple layers of copper paints. We note that a layer of primer should be applied before the deposition, which is a key step to improve the adhesion of the copper paint to the TTZ material.

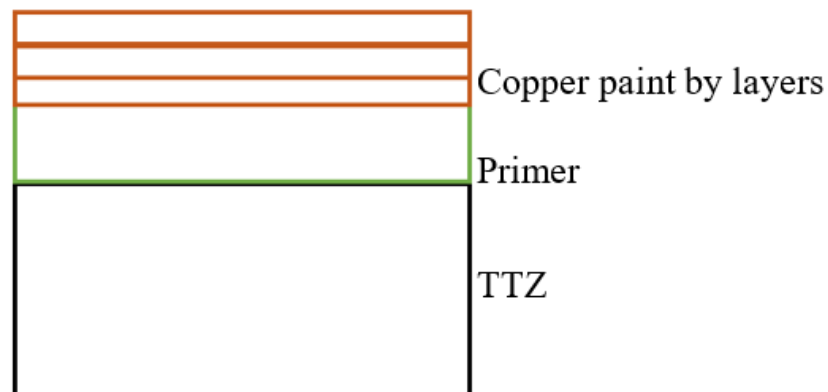


Figure 14: Copper paint deposition technique

Nevertheless, the copper paint also had some disadvantages when preparing the interface between the plates and the feed structure. The surface of the copper paint is too soft and cannot stand high temperature. This created an issue when the plates were soldered to the paint surface.

Table 1 summarizes the advantages and disadvantages of the two approaches.

| APPROACH | ADVANTAGES | DISADVANTAGES |
|---------------------|---|---|
| COPPER TAPE | <ul style="list-style-type: none"> - Cheap - Easy to use - Good interfacing with different material - Can hold high temperature (soldering) | <ul style="list-style-type: none"> - Poor adhesion - Cannot be submerged in oil for a long time |
| COPPER PAINT | <ul style="list-style-type: none"> - Can be used in oil - Good adhesion | <ul style="list-style-type: none"> - Cannot hold high temperature (soldering) - Soft surface - Expensive - Requires multiple procedures |

Table 1: Design approach differences

Despite the fact that copper paint has a good adhesion to the surface, it is quite challenging with interfacing copper paint with the feed structure, so we instead used the copper tape. The poor adhesion can be fixed by applying a thin layer of epoxy glue on the plate edges to protect the plates from exposure to oil. After the plates were created and taped to the antenna body, a resistor ring was fitted to the antenna emitting section. The final antenna can be seen in Figure 15.



Figure 15: Constructed antenna model with resistor ring

2.3 Feed Structure

As mentioned previously, the antenna was designed for delivering pulses to biological targets. This particular application requires high voltage pulses to feed into the antenna so the feed structure is crucial to the antenna operation. Two parallel plates with a Teflon dielectric liner were chosen because they provide some space between the plates and can prevent the breakdown at the tip of the antenna when high voltage is applied. Another advantage of this type of feed is it maintains a balance field along the plates. This will contribute a uniform field to the antenna. The parallel plates feed a structure that consists of two sections. Section 1 is the coaxial cable. Section 2 is the parallel-plate feed.

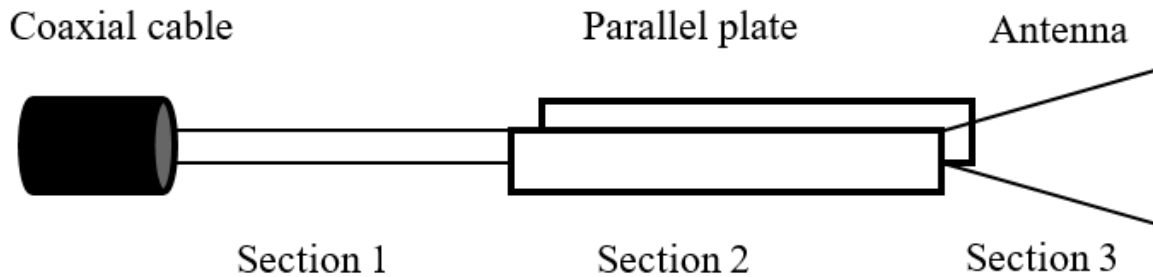


Figure 16: Parallel plates feed structure

In Section 1, the coaxial cable connecting the power source was RG217. A typical coaxial cable is shown in Figure 17. [30]

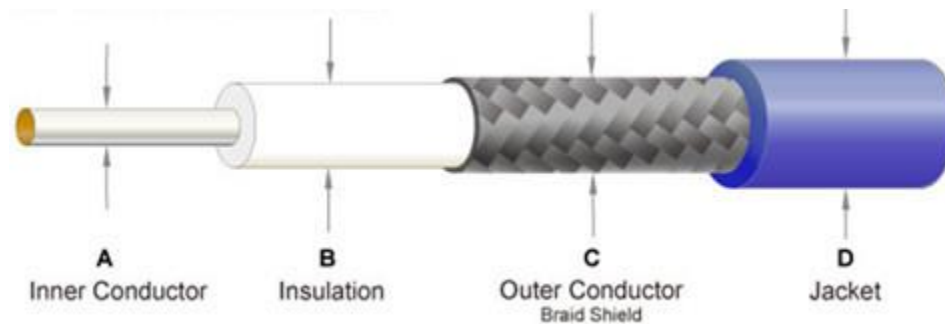


Figure 17: Coaxial cable breakout [30]

In order to connect the coaxial cable to the parallel plates, the jacket of the cable has to be removed. The inner and outer conductors of the coaxial cable are acting as the positive and negative terminal which will then be connected to the parallel plates. The impedance of the coaxial cable is 50Ω , so it matches the impedance of the plates and the antenna impedance.

For a given Teflon sheet that has the thickness of 0.8 cm, in order to determine the dimension of the parallel plates, an impedance formula is applied:

$$Z_0 = Z_c \left(\frac{d}{w} \right) \sqrt{\frac{\mu_r}{\epsilon_r}} \quad [31-32] \quad (14)$$

Where Z_0 is the parallel plates' impedance

Z_c is the impedance in free space

d is the gap distance

w is the width of the parallel plates

μ_r is the relative permeability

ϵ_r is the relative permittivity

In this case, the gap distance was 0.8 cm, $Z_c = 377$ ohms, $Z_0 = 50$ ohms, $\mu_r = 1$ in air, and $\epsilon_r = 2.1$. So the width of the parallel plates was determined to be 4.16 cm. In this case, the length and the thickness of the parallel plates are neglected. In order to hold the parallel-plate structure in place a 3D printed holder was manufactured. The feed structure and the antenna were soldered to prevent the impedance discontinuity. Furthermore, epoxy glue was applied to stabilize the coaxial cable and the antenna. The completed feed structure with the antenna is shown in Figure 18.

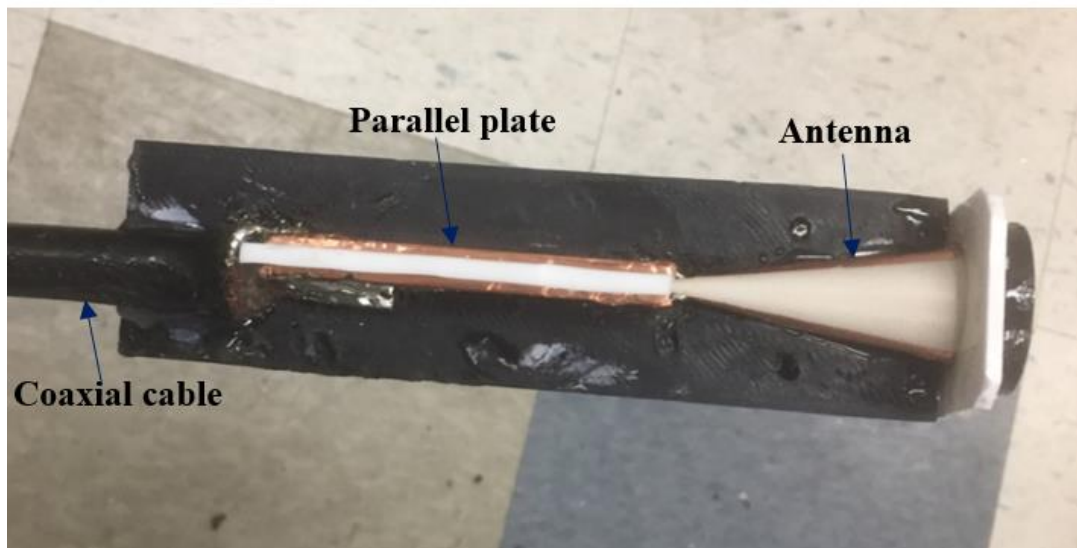


Figure 18: Constructed parallel feed structure

2.4 3D Simulations

To have a grasp of how the antenna works, a series of 3D simulations were performed. The antenna was simulated for two different conditions. The first was that the antenna was immersed in water. The electric field was probed at 1mm, 2mm, 3mm, 4mm, 5mm, 10mm, and 20mm away from the wave emitting section. The input signal of the simulation is a default Gaussian waveform with the magnitude of 1 V. The 3D simulation from CST can also display how the electric field travels from the excitation port through the antenna and emits to the target. The second condition was that the antenna was immersed in oil with the rest of the conditions remaining the same.

The two scenarios (Figure 19) were simulated in order to compare with the experimental results and validate the performance of the antenna. The choice of water and oil was because they could prevent and suppress the high voltage breakdown at the tip of the antenna.

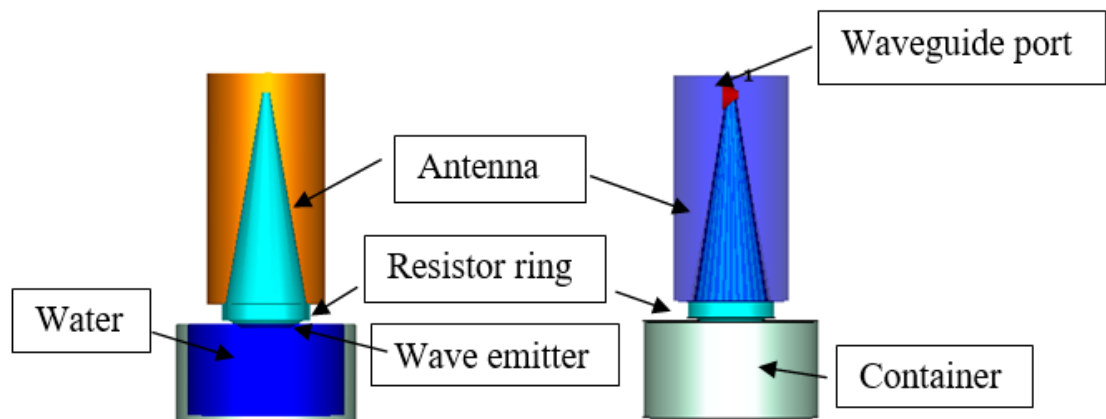


Figure 19: Antenna 3D simulation model

Table 2 summarizes the field values at different distances from the antenna.

| PROBES DISTANCE(MM) | ELECTRIC INTENSITY(V/M) IN WATER | FIELD IN OIL | ELECTRIC INTENSITY(V/M) IN OIL | PERCENTAGE DIFFERENCES (%) |
|---------------------|----------------------------------|--------------|--------------------------------|----------------------------|
| 1 | 18.681 | 26.29 | | 28.9 |
| 2 | 16.811 | 24.126 | | 30.31 |
| 3 | 15.048 | 22.167 | | 32.11 |
| 4 | 13.493 | 20.283 | | 33.47 |
| 5 | 12.132 | 18.492 | | 34.39 |
| 10 | 7.89 | 12.583 | | 37.29 |
| 20 | 5.44 | 7.40 | | 26.34 |

Table 2: 3D Simulation Results at different distance

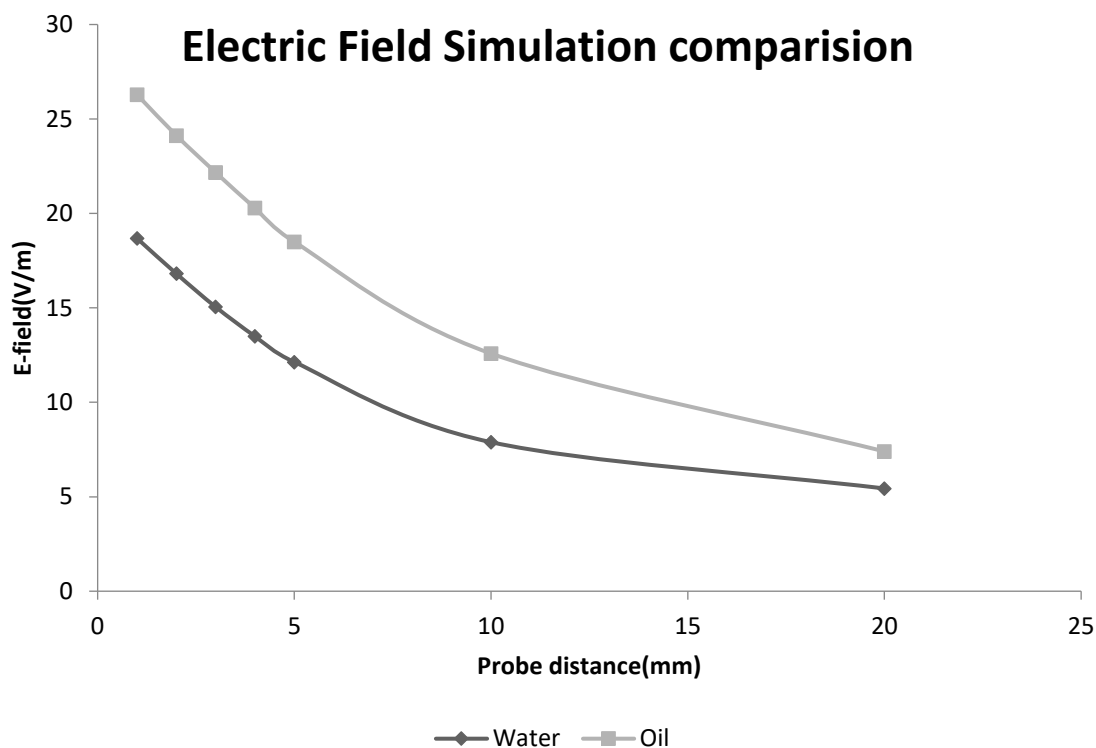


Figure 20: Electric Field Simulation in water and oil

The electric fields for both conditions show similar characteristics. They have the same decay trend. The field is higher at nearer distances to the antenna tip but it levels out after 1cm. The results show that the magnitude of the electric field for the oil case is 31.83% higher than that for the water case.

Figure 21 shows how the field travels from the antenna source. Before 1 ns, the electric field is mostly guided by the antenna, but there is also an electric field that travels faster outside the antenna, which does not contribute to the overall field at the target because it is much weaker than the one guided by the antenna. At 1.5 ns, there is a pulse at a depth of approximately 1 cm, which continuously travels deeper but its intensity decreases rapidly. In general, the antenna is not efficient with much of the electric field reflected back to the source.

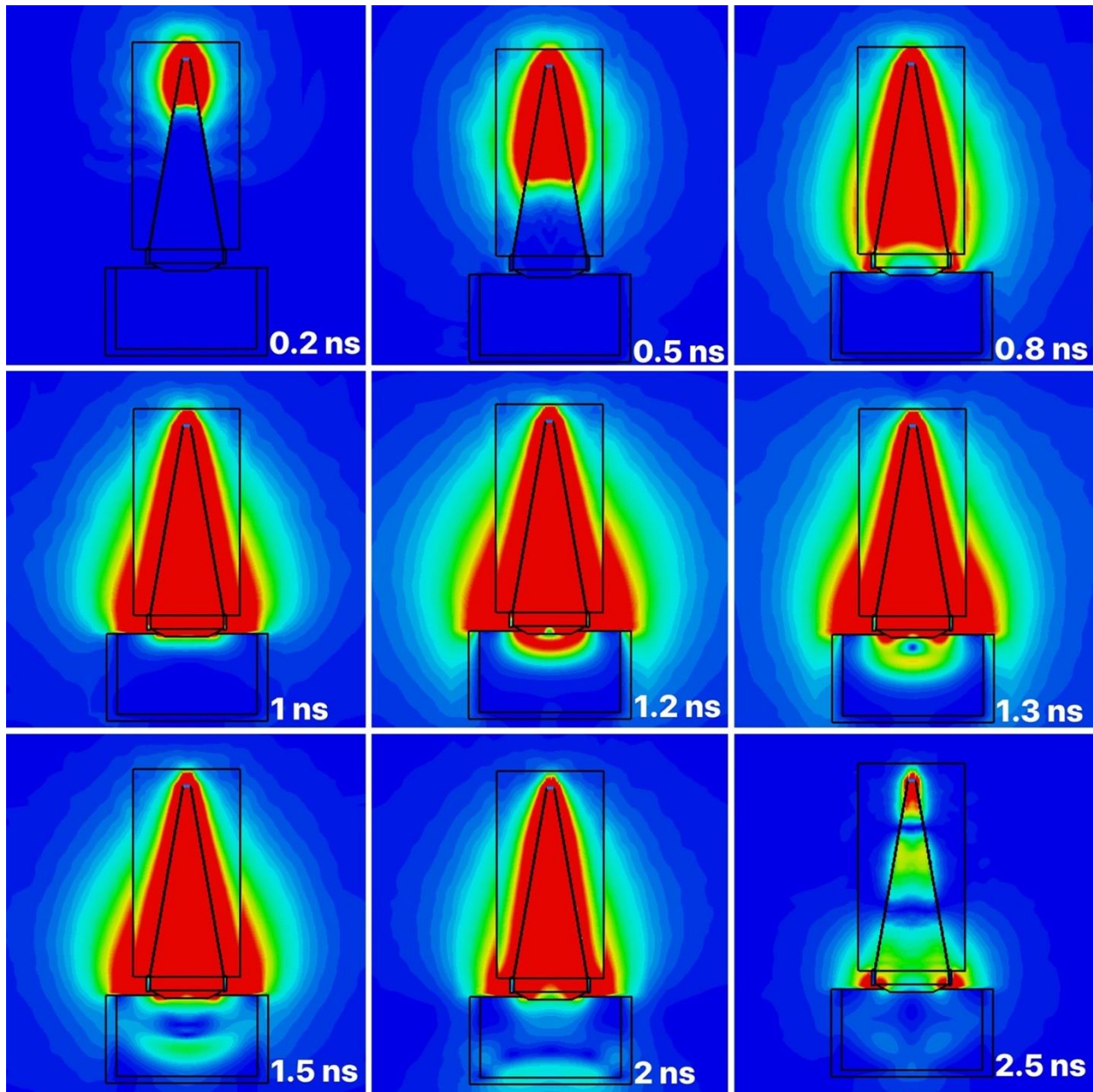


Figure 21: 3D Simulation (E-field) in oil

The simulations were made to investigate the direction of the fields along the antennas structure. Results were taken for different time points from 0.2 ns to 2.5 ns.

In the antenna, the direction of the field is horizontal. The direction remains unchanged until the wave reaches the emitting section. A closer examination shows that the radiated wave has the same direction as the original wave port excitation signal.

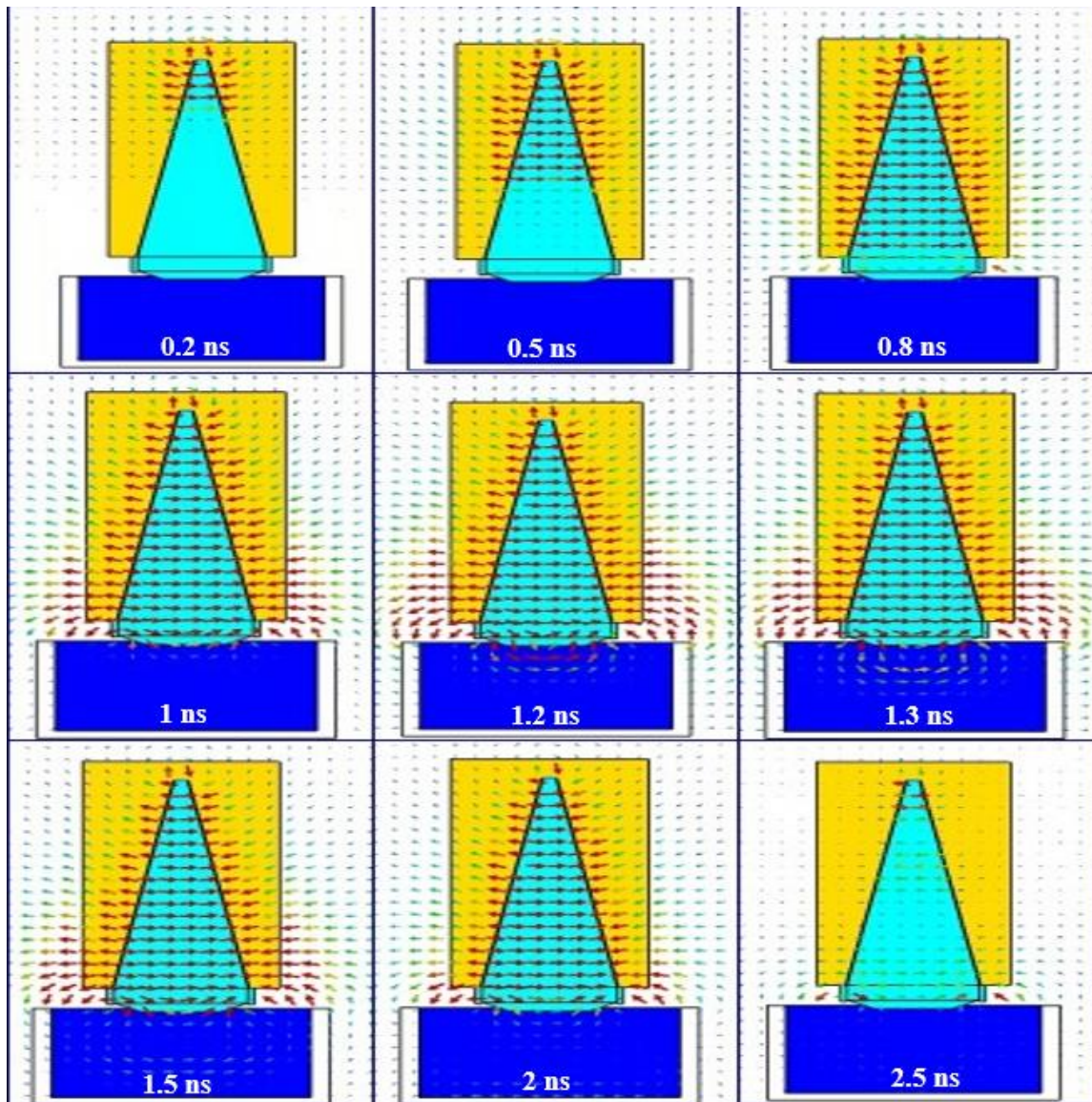


Figure 22: E-field Direction in oil

Another simulation was made to determine the direction of the magnetic field. In theory, the magnetic field is perpendicular to the electric field, and the direction of the magnetic field can be determined by the right hand rule according to the power flow direction. Since the direction of

the electric field is known, the magnetic field is expected to point outward. Figure 23 verifies the direction of the magnetic field.

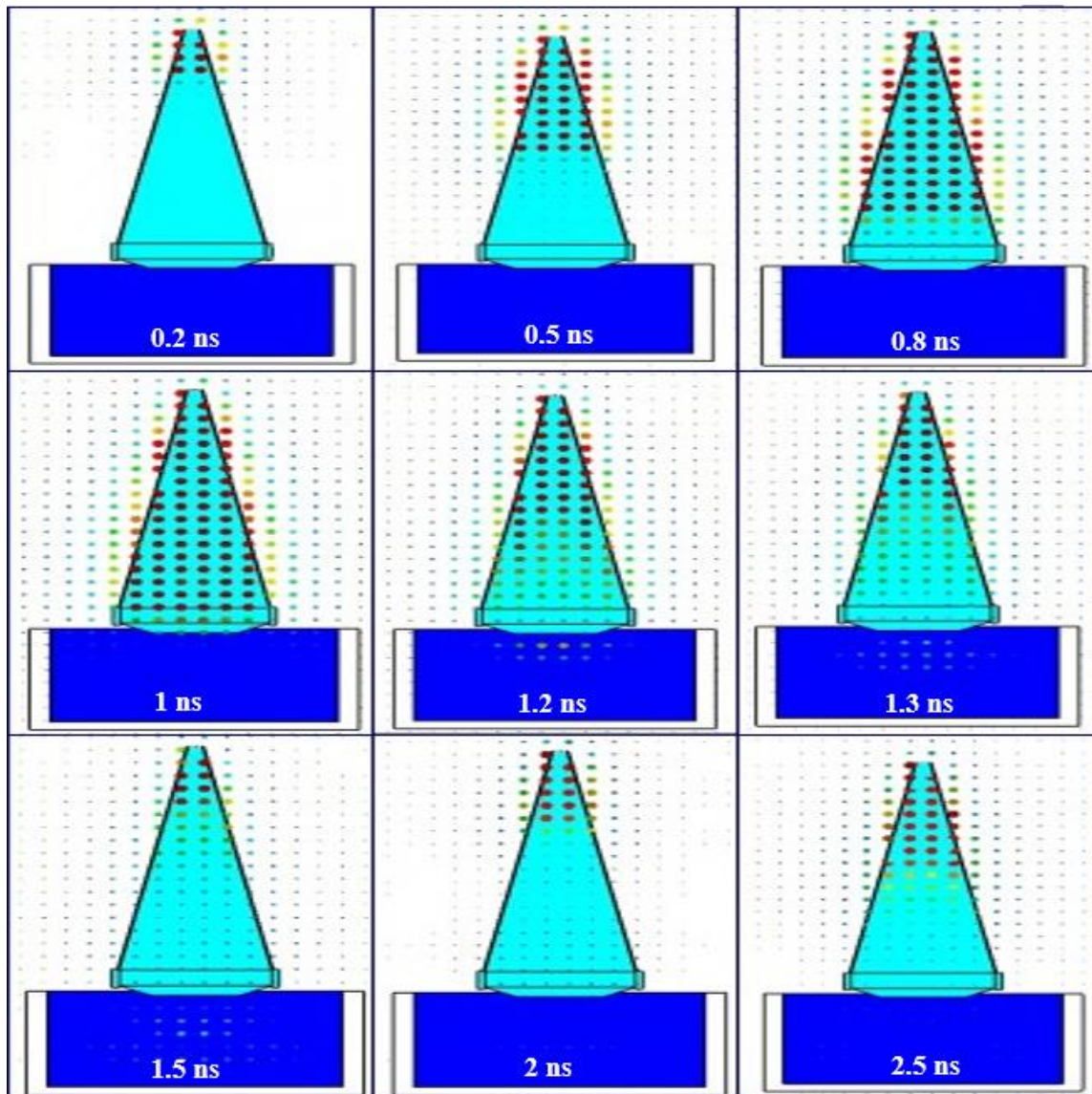


Figure 23: H- field Simulation in oil

Next, a simulation was made to determine the surface current distribution. The direction of the current can also be determined using the right hand rule (Ampere's Law). The current is expected to flow from left to right across the wave port signal (Figure 24).

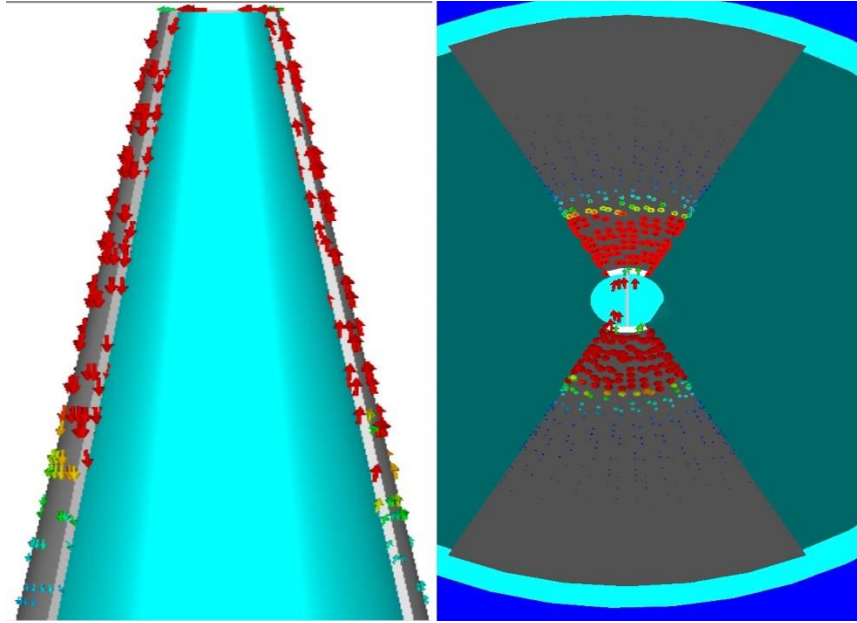


Figure 24: Current distribution of the PEC triangular PEC cone.

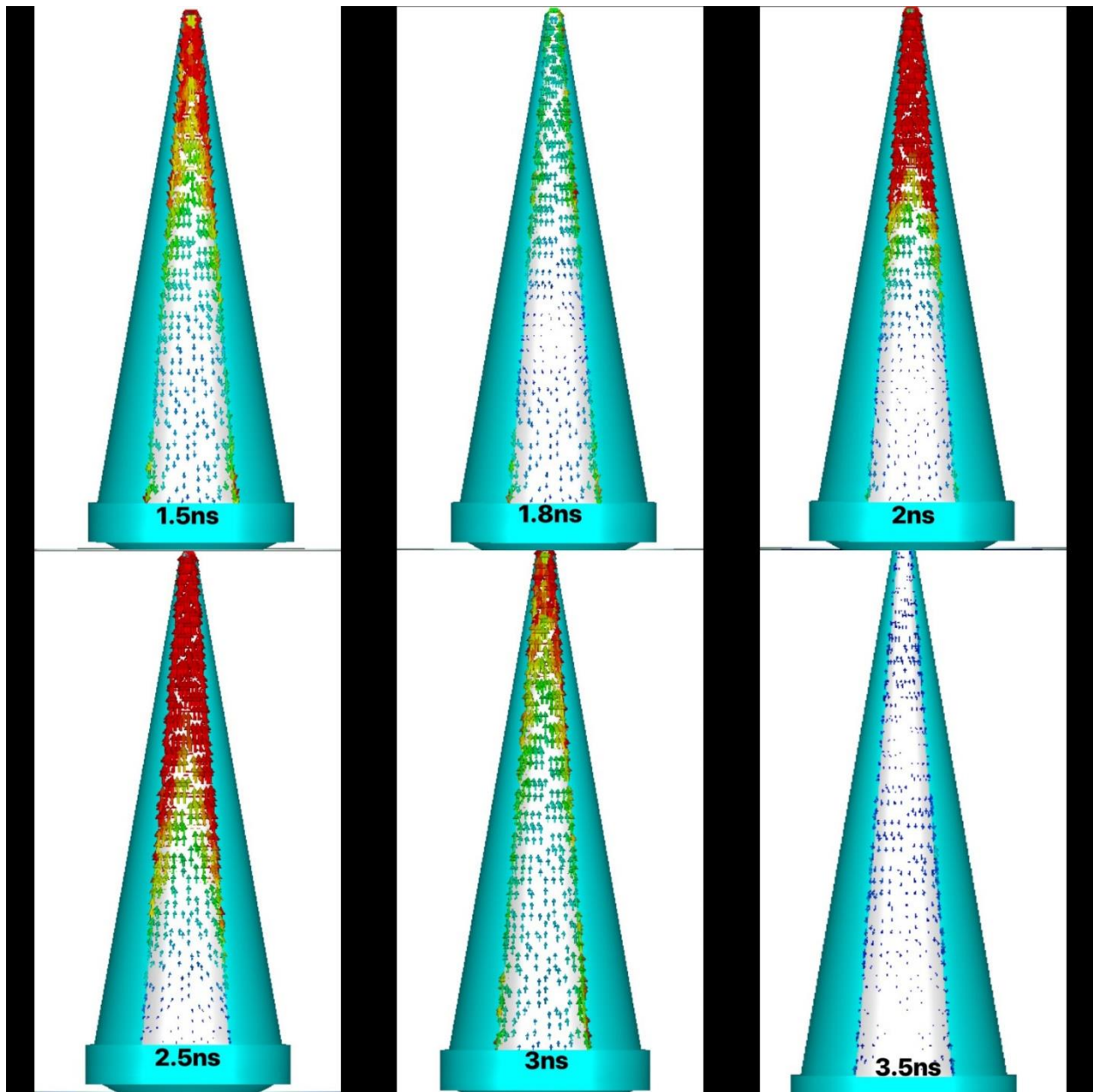


Figure 25: Current flow after the wave is radiated

Figure 25 shows a current flow for a travelling wave at 1.5 ns, 2.5 ns, and 3 ns, for which the current direction throughout the plates is uniform although the intensity is not necessarily uniform. The current that has a standing wave feature is shown at 1.8 ns and 2 ns, for which two current directions coexist on the plate. This observation suggests the impedance of the antenna is not matched completely and therefore causes a strong return to the source. The overlapping of

the forward wave and backward wave causes zero current. But the location of the zero current is not at the antenna emitting section, which is beneficial for the antenna radiation.

Finally, a simulation was made to determine the importance of the resistor ring.

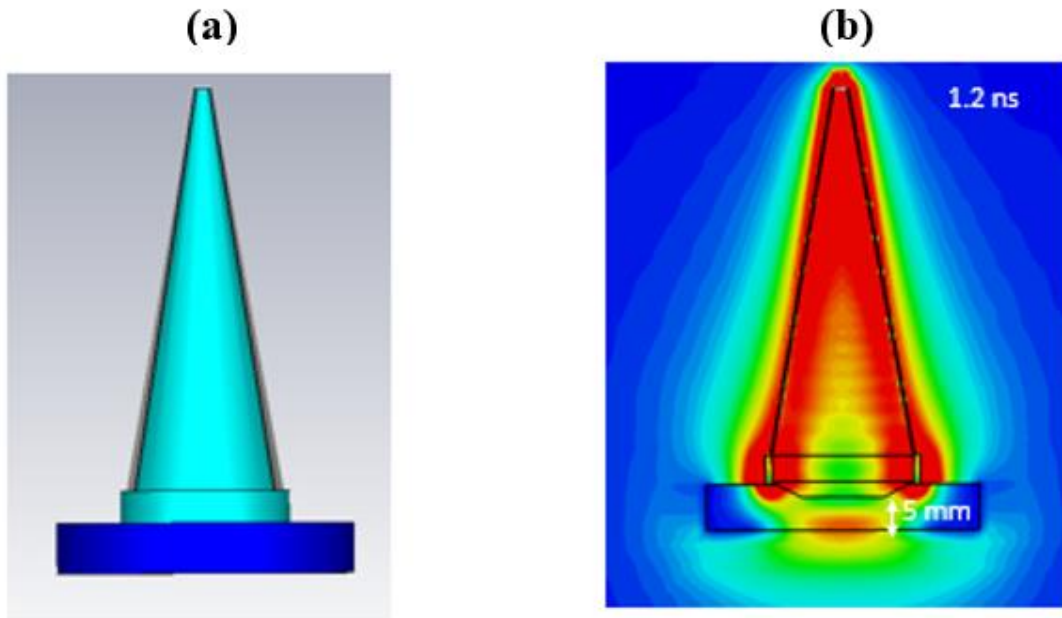


Figure 26: a) Antenna 3D model. b) E-field simulation at 1.2 ns.

The results show that the antenna is able to deliver a pulse to a target at a depth of 5 mm at 1.2 ns (Figure 26b). The field is largely confined to the center of the antenna (Figure 27).

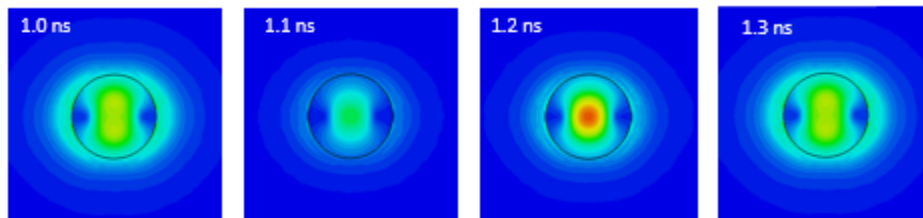


Figure 27: Produced electric field at specific time and its focal point

Figure 28a shows the electric field is much higher with the resistor ring than that without. The pulse width is also longer. This waveform reflects that the field consists of two parts: 1) the radiated field, which is proportional to the time derivative of the input pulse (in this case, it is a ramp pulse) and 2) the original pulse. The second pulse is only seen when the resistor makes contact with water. The first part is the result of the displacement which counts towards the radiation term and the second part is the result of current conduction through a resistive path.

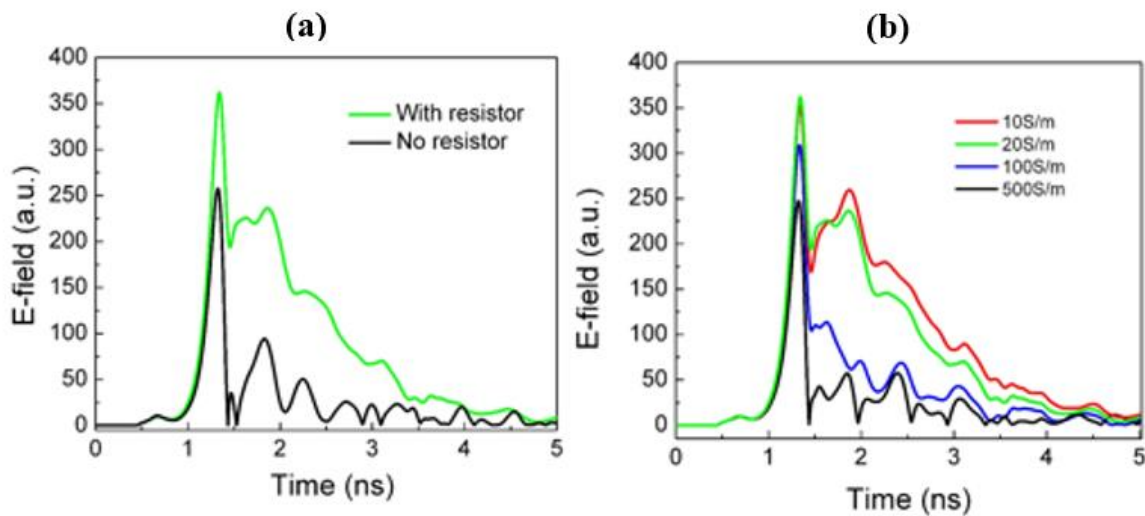


Figure 28: a) Produced E-field with and without the resistor ring. b) Produced E-field of various conductance values.

2.5 Experimental Setup

The antenna was tested with various input voltages ranging from a few kV to 50 kV, because the power supplies were different. The experiment for low voltages was set up with the feed structure and the antenna both under water. The electric field probe, which is fiber optic based (see appendix), was placed underneath the wave emitting section. Furthermore, the probe was placed to be orthogonal to the two triangular plates in order to measure the full field level (Figure 29).

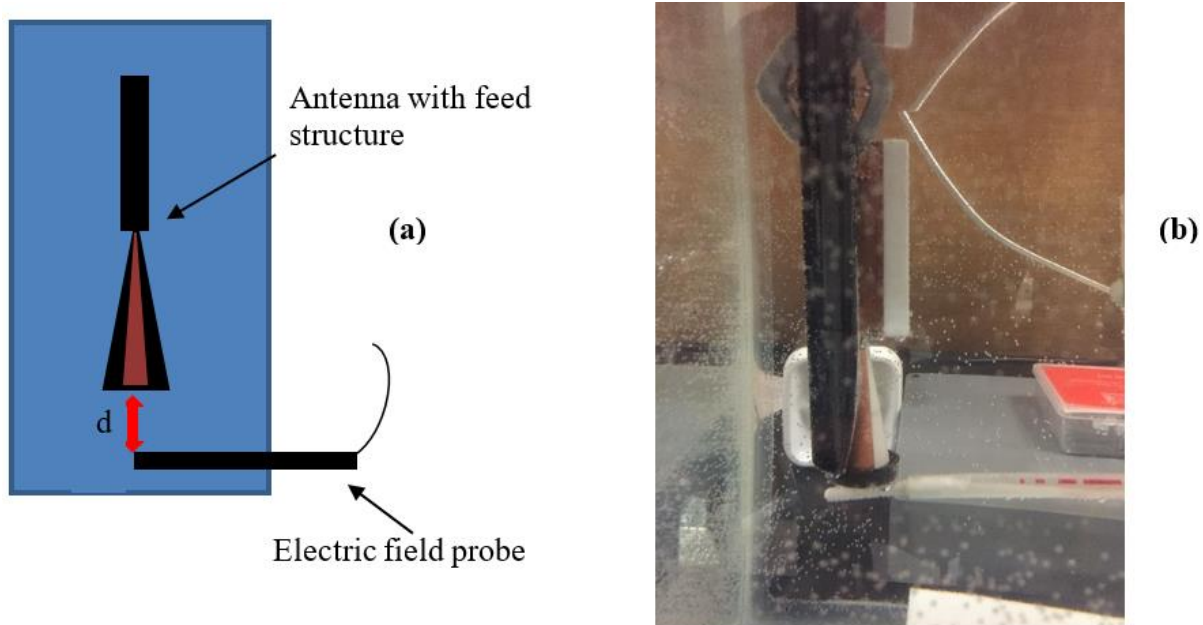


Figure 29: a) Schematic for experimental setup for voltage testing b) Experimental picture for low voltage testing.

The distance (d) between the antenna and the probe was set for 2mm, 5mm, 10mm, and 20mm.

For high voltage testing (>30 kV), a special antenna housing was constructed to prevent potential voltage breaking down. An acrylic bottle was used to contain the antenna when oil was filled in. A circular hole was made to let the resistor ring and the wave emitting section be exposed outside of the bottle. In order to prevent leaking of the bottle design, epoxy glue was used to seal the space between the antenna and the bottle. Figure 30 shows the completed antenna.



Figure 30: Antenna structure with a bottle housing

In testing the antenna, the antenna emitting section was dipped in water. The electric field probe was placed underneath the wave emitting section, also orthogonal to the triangular plates. As soon as the probe was secured, water was added to the tank until it reaches the wave emitting section. Avoiding water to touch the resistor ring was necessary because it ensures that only the radiative term was measured. The probe was positioned for distances 2mm, 5mm, 10mm, and 20mm.

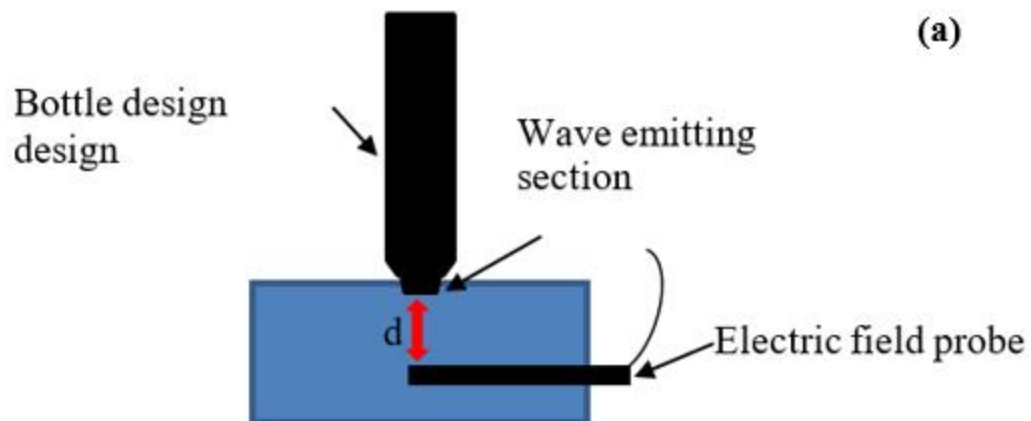


Figure 31: a) Schematic for experimental setup for high voltage testing b) Experimental picture for high voltage testing

2.6 Experimental Results

At low voltage experiments, the input voltages were 1, 5, and 10 kV. The measurement were performed at 5mm, 10mm, and 20mm. Figure 32 is the waveform of the measurement, obtained at 10mm distance with a 10 kV input voltage. Figure 32 shows a sample waveform of the produced electric field. The characteristics of the waveform remained similar at various input voltages. The differences were in the magnitude of the waveform.

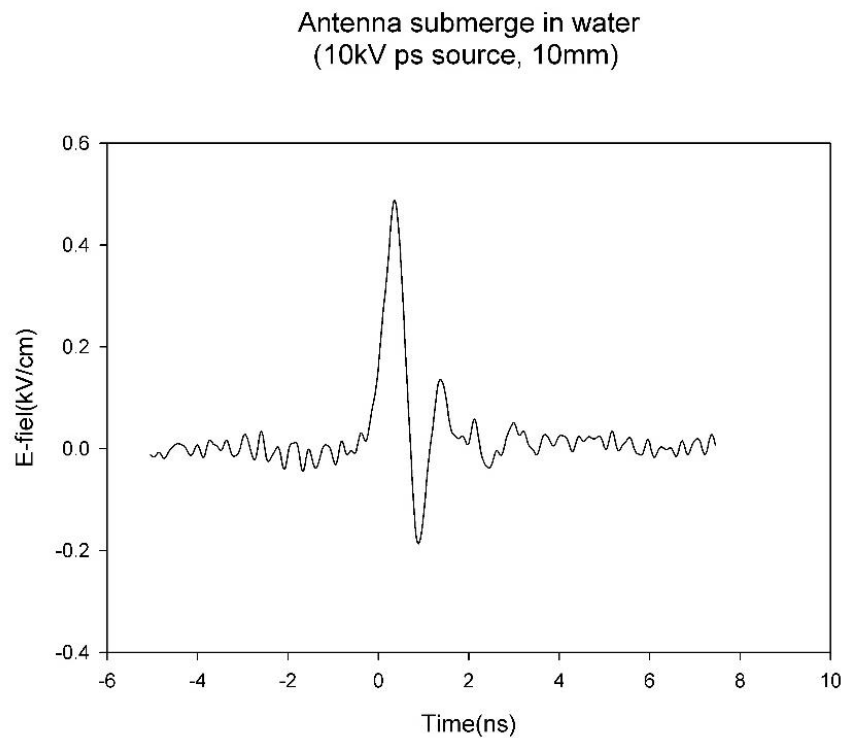


Figure 32: Antenna waveform at 10mm gap distance and 10kV input voltage is applied

| INPUT VOLTAGE(KV) | DISTANCE(MM) | OUTPUT E-FIELD(KV/CM) |
|-------------------|--------------|-----------------------|
| 1 | 5 | 0.0648 |
| 1 | 10 | 0.048 |
| 1 | 20 | 0.03816 |
| 5 | 5 | 0.324 |
| 5 | 10 | 0.246 |
| 5 | 20 | 0.156 |
| 10 | 5 | 0.5808 |
| 10 | 10 | 0.4776 |
| 10 | 20 | 0.3024 |

Table 3: Low voltage experimental results at different input voltages with various distances

Table 3 summarizes the results at various distances. Due to the restriction of equipment, the data points cannot go any lower than 5mm. However, the trend line of the output electric field is similar to the simulation data. Figure 33 shows the trend lines for 3 different voltages.

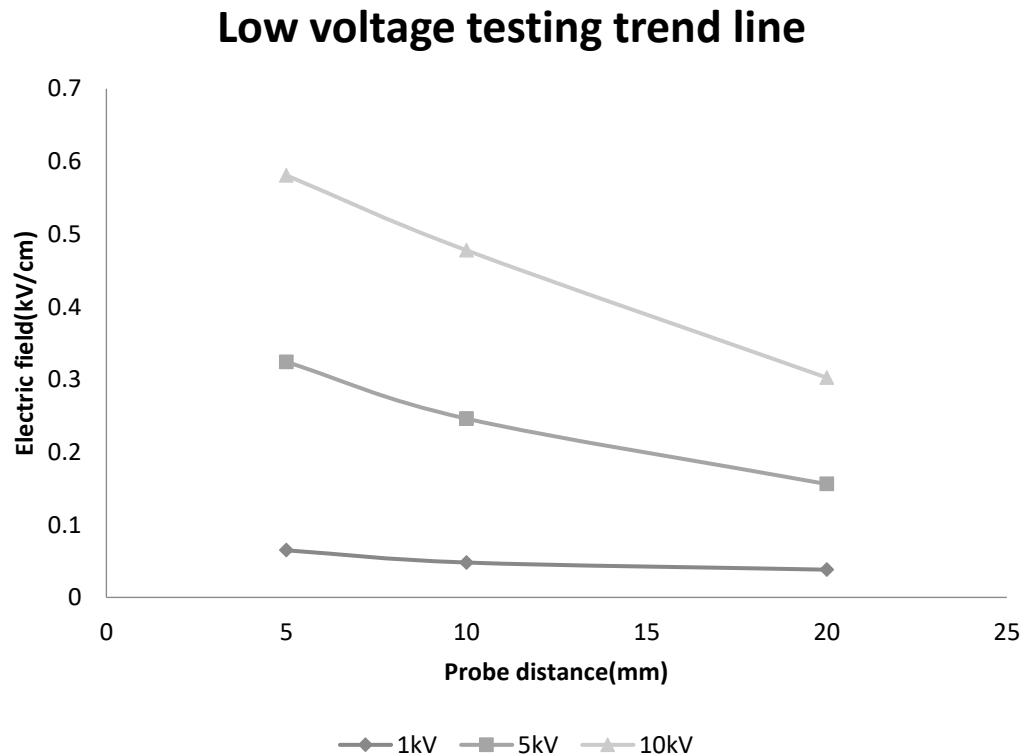


Figure 33: Low voltage trend line at different testing input voltages

Since the low voltage testing is performed under water, we compare the results with the simulation data. By observation, the characteristic of the trend line of the experimental data does not follow the 3D simulation. However, the magnitude is far less than the simulated data. According to the simulation, the antenna should produce 12.132 V/m for 1 V input, which means 0.6kV/cm for 5 kV input. However, the experimental data only shows 0.324kV/cm, which is almost two times less.

In order to determine the characteristic of the antenna at high voltages, a series of experiments were performed from 30 to 50 kV, with a voltage step of 5kV. The experiments were performed at four different distances, 2mm, 5mm, 10mm, and 20mm. Table 4 shows the collected data.

| INPUT VOLTAGE(KV) | DISTANCE(MM) | OUTPUT E-FIELD(KV/CM) |
|--------------------------|---------------------|------------------------------|
| 30 | 2 | 1.512 |
| 30 | 5 | 1.404 |
| 30 | 10 | 1.056 |
| 30 | 20 | 0.768 |
| 35 | 2 | 1.512 |
| 35 | 5 | 1.488 |
| 35 | 10 | 1.224 |
| 35 | 20 | 0.924 |
| 40 | 2 | 1.512 |
| 40 | 5 | 1.524 |
| 40 | 10 | 1.356 |
| 40 | 20 | 1.032 |
| 45 | 2 | 1.512 |
| 45 | 5 | 1.548 |
| 45 | 10 | 1.416 |
| 45 | 20 | 1.092 |
| 50 | 2 | 1.512 |
| 50 | 5 | 1.548 |
| 50 | 10 | 1.44 |
| 50 | 20 | 1.14 |

Table 4: High voltage experimental results at different input voltages (30-50 kV) with various distance (2-20mm)

Figure 34 shows the trend of the fields at different voltages and distances. Interestingly, all the fields at different voltages for the closest distance (2 mm) converge to the same field (1.5kV/cm). This is very likely caused by the saturation of probe. Such saturation caused the nonlinear trend line, which shouldn't exist for lower feed voltage.

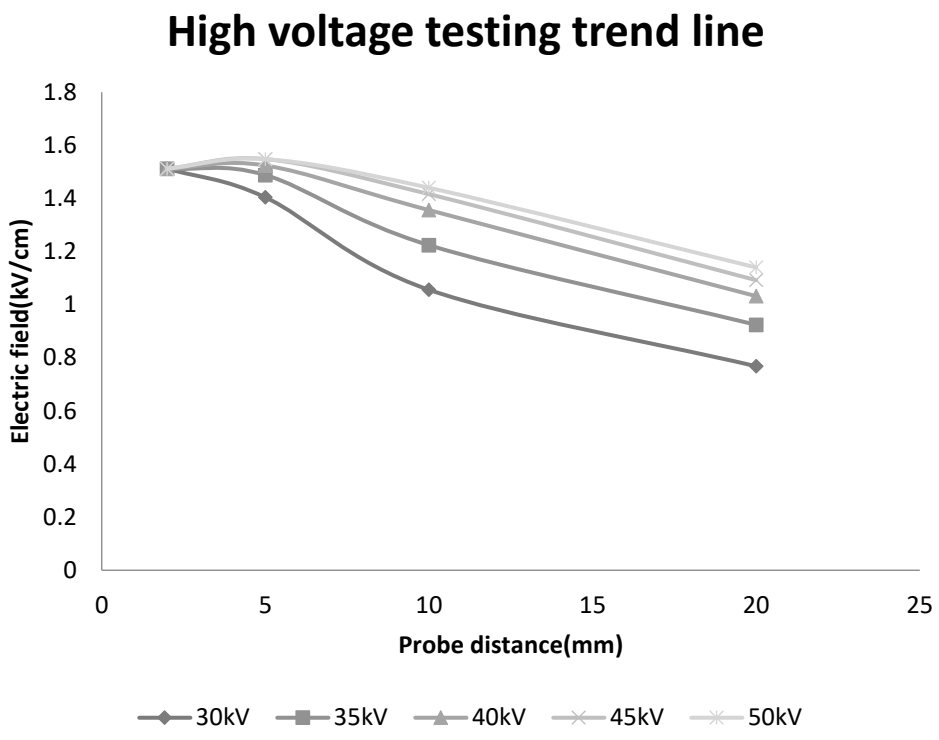


Figure 34: High voltage trend line at different testing input voltages

We combined the results in both low and high voltage experiments. Since there are no readings at 2mm at low voltage, the results are shown only at 3 different distances, which are 5mm, 10mm, and 20mm (Figure 35).

Antenna Experimental Data

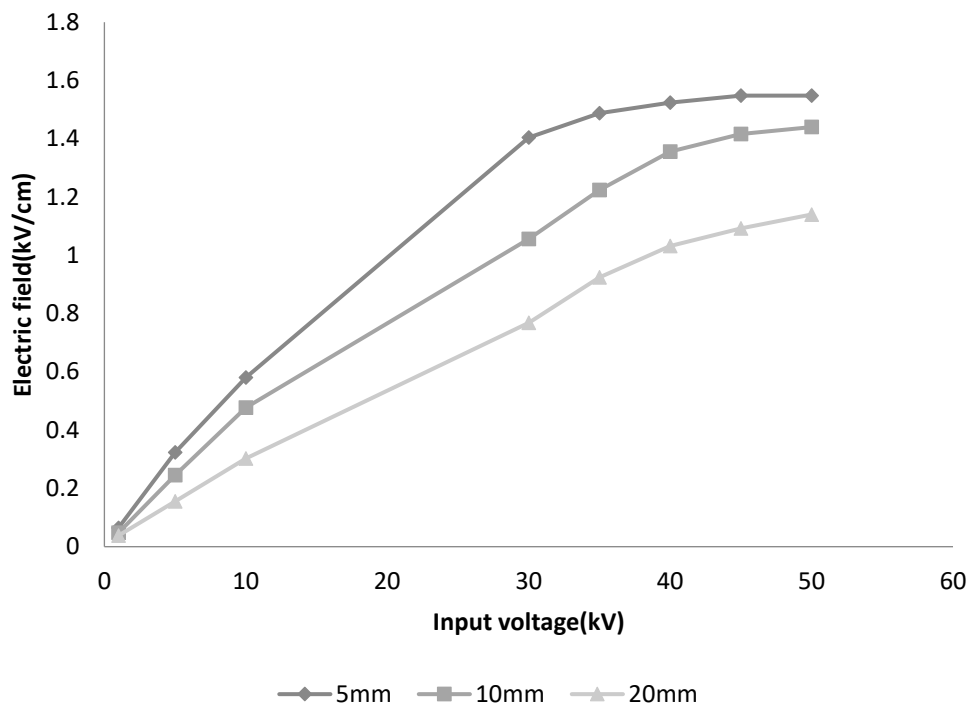


Figure 35: Experimental results trend line at 5, 10, and 20 mm

Figure 35 shows that the antenna's electric field has a slight increase as the input voltage increases. It also shows that the closer it is to the wave emitting section the stronger electric field it gets. Furthermore, the trend line (at 5mm) starts to saturate when the input voltage increases from 30 kV to 50 kV. The saturation can be observed when the 10mm trend line reached 40-50kV. Similarly, the 20mm trend line also shows the presence of saturation for a voltage from 40-50 kV. These data suggests that there is another saturation besides the probe saturation. This could be that the antenna dielectric couldn't hold its dielectric value at high voltages.

2.7 Summary

Table 5 summarizes the comparison of simulation versus experimental results. In short, the measured electric field is less than the simulation result. The difference is larger as the input voltage becomes larger. This is most likely due to the dielectric failure, which points to changing the material of the antenna in order to improve the antenna efficiency.

| INPUT VOLTAGE(KV) | SIMULATED RESULT(KV/CM) | EXPERIMENTAL RESULT(KV/CM) | DIFFERENCES(TIMES) |
|--------------------------|------------------------------------|---------------------------------------|---------------------------|
| 1 | 0.12132 | 0.0648 | 1.87 |
| 5 | 0.606 | 0.324 | 1.87 |
| 10 | 1.2132 | 0.5808 | 2.08 |
| 30 | 5.5476 | 1.404 | 3.95 |
| 35 | 6.4722 | 1.488 | 4.34 |
| 40 | 7.3968 | 1.524 | 4.85 |
| 45 | 8.3214 | 1.548 | 5.37 |
| 50 | 9.246 | 1.548 | 5.97 |

Table 5: A comparison of simulation and experimental results with different input voltage

Chapter 3. A Pulse Transformer

The concept of a dual resonant air core pulse transformer (DRPT) was adapted from a previous design [34]. The rationale of this transformer is to produce a high voltage but ultrafast charging pulses. The produced pulses can be integrated with an antenna to form a complete EMP system.

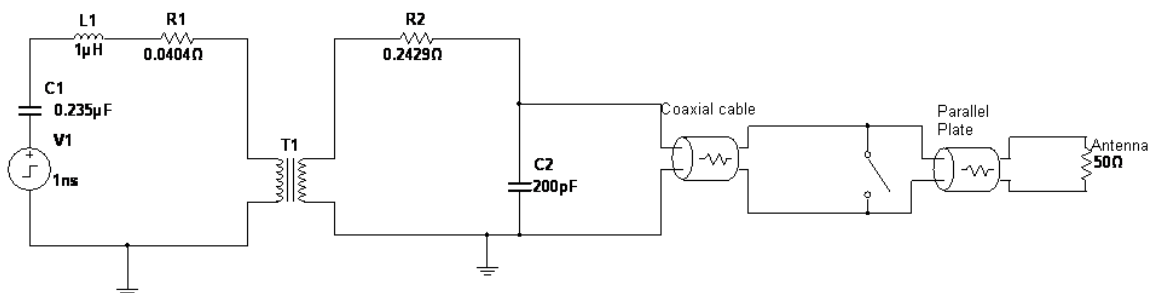
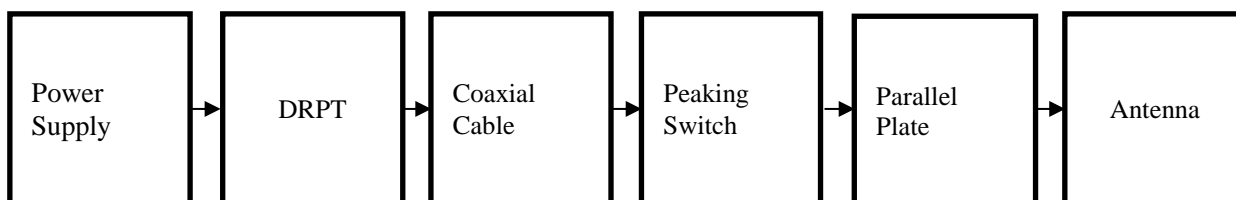


Figure 36 shows the whole system. The sequence begins with the primary capacitor (C1). The energy is transferred to the primary inductor (L1). Next, the energy from the primary is converted to the secondary following the basic concept of a transformer. Furthermore, the secondary capacitor and inductor are charged. When the energy arrives at the switches, this will shorten the pulses' width of the transformer's outputs waveform. The peaking switch breaks down very fast and produces pulses in picosecond range. The antenna can radiate the pulses.



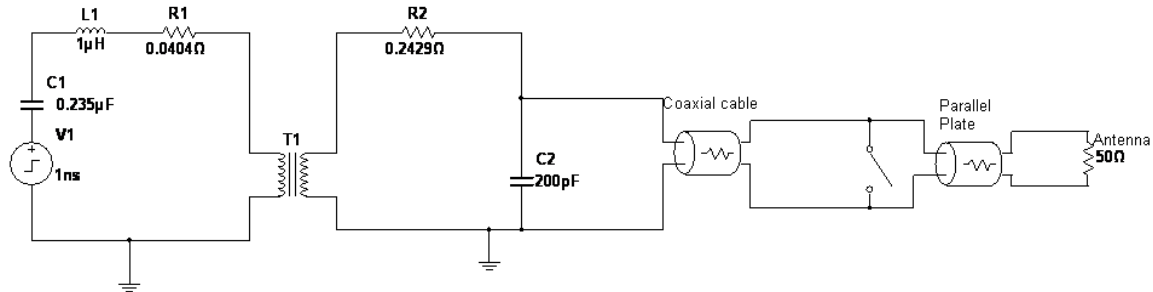


Figure 36: Block diagram and circuit diagram of a DRPT

In this chapter, the following section will introduce the transformer. The construction procedure is also presented, followed by Multisim simulation. The simulation model was made to predict the gain, and the transient characteristic of such transformer. Experiments were performed to measure the gain.

3.1 A DRPT

A DRPT is typically used to charge a capacitive load. The advantages of this type of transformer are low-cost, easy to be built, and compact. Furthermore, the absence of the magnetic core will prevent core saturation. Another plus is it can operate without limited frequency. Since there is no magnetic core, the coupling coefficient of the air core transformer is lower than the one that has. A DRPT has to follow the convention that the product of the primary has to match the secondary ($L_1 C_1 = L_2 C_2$)[31-35].

The matching of frequency is optimal for a maximum energy transfer. The charging can take place in two cases. The first is charging in the first peak. The secondary is charging at the second peak. The second case is the dual-resonance charging (Figure 37).

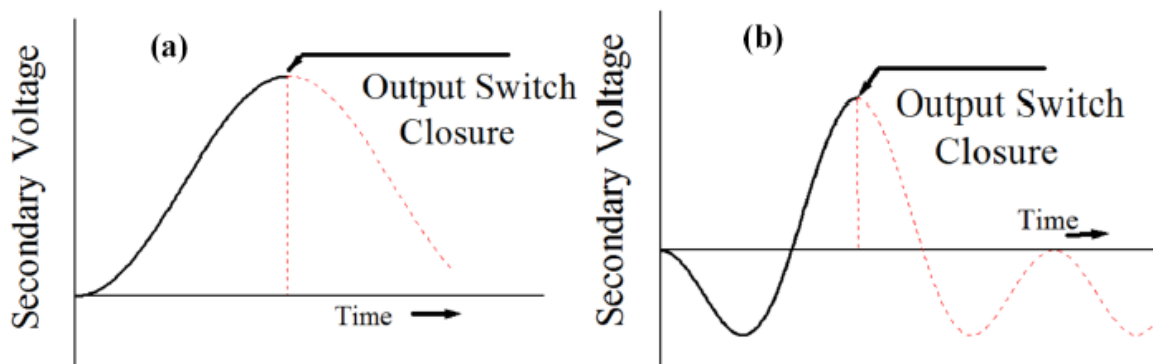


Figure 37: a) First swing charging cycle. b) Dual resonant charging cycle. [35]

Depending on the winding method, there are two types of air core transformers. The first type of transformer is the spiral/strip transformer, or Rohwein spiral-strip transformer. The other one is the helical wire/strip transformer, which is mainly discussed in this chapter. In the design of the thesis, the primary was wound around a thick PVC pipe, with a right dimension to fit the secondary pipe inside. The secondary was made from wires winding around a smaller PVC pipe. PVC pipes were chosen as insulators to prevent high voltage breakdown [34].

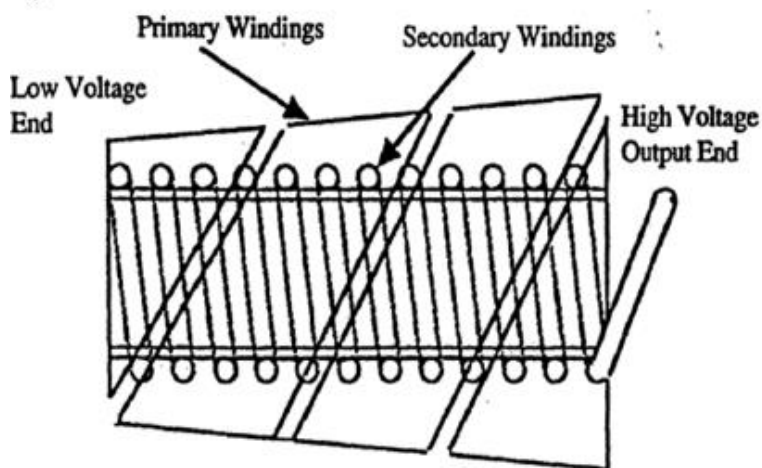


Figure 38: Helical wire/strip transformer [35]

This transformer circuit consists of a primary capacitor (C1), primary inductor (L1), secondary capacitor (C2), and secondary inductor (L2) (Figure 39). The primary and secondary inductors are mutually coupled. The number of turns, or the amount of inductances are correlated with the gain of the transformer.

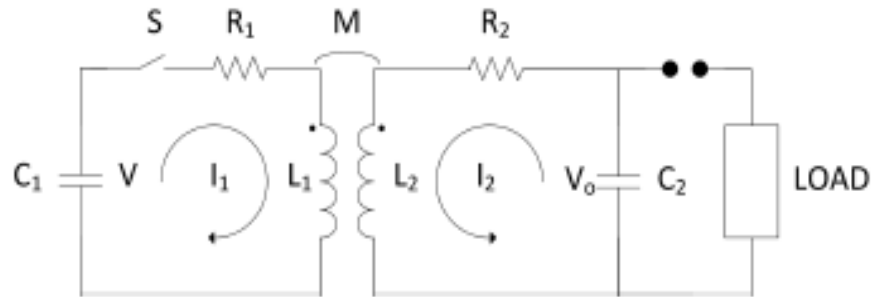


Figure 39: A DRPT equivalent circuit [35]

When the primary stage is closed and current starts to flow, the voltage across C2 is a function of time: [29-36]

$$V_0(t) = \frac{Vk}{C_2\sqrt{L_1L_2}} \frac{\cos(\omega_b t) - \cos(\omega_a t)}{\omega_a^2 - \omega_b^2} \quad (15)$$

where,

$$\omega_a^2 - \omega_b^2 = \left[\frac{(L_1 C_1 - L_2 C_2)}{2(1-k^2)} \pm \left(\frac{1}{2(1-k^2)} \right) \sqrt{(L_1 C_1 - L_2 C_2)^2 - 4(1-k^2)(L_1 C_1)(L_2 C_2)} \right] \quad (16)$$

$$k = \frac{M}{\sqrt{L_1 L_2}} \quad (17)$$

Since the first voltage swing will not be the maximum due to the under coupled condition, the maximum voltage occurs at the second peak. This follows the dual resonance charging as seen in Figure 37b.

In the air-core transformer design, a desired waveform can be created by focusing the times of the first and second peak, which relates to the maximum theoretical gain. The occurrence of the first two peaks is related to [34, 35]

$$\tau_1 = \frac{\pi}{2\sqrt{L_1 C_1}} \text{ and } \tau_2 = \frac{3\pi}{2\sqrt{L_1 C_1}} \quad (18)$$

Since $L_1 C_1 = L_2 C_2$, the occurrence of the first two peaks can also be calculated using the values of the secondary. And, the maximum of the second peak is related to the voltage gain:

$$V_0 = V \sqrt{\frac{L_2}{L_1}} = V \sqrt{\frac{C_1}{C_2}} \quad (19)$$

This is an ideal case. The actual gain of the transformer has the gain of approximately $(0.2 - 0.4) \sqrt{\frac{L_2}{L_1}}$ due to the under coupled condition, magnetic flux leakage, and parasitic values [29-36].

3.2 Construction of transformer - Design 1: Helical Configuration

The construction of this transformer took two steps. The first was the primary inductor coil. A large aluminum foil that has a width of 0.114 meters and a length of 0.3 meters was chosen, which was wrapped around a 4.5 inch pipe with a length of 15 inches. After wrapping the foil around the pipe, the number of turn of the primary is approximately 2.41 turns. The second step of the construction was to build the secondary coil. A PVC pipe with a diameter of 3.6 inches and a length of 12 inches was chosen to fit inside the primary coil PVC pipe. The Gauge 8 wire

was used to wind around the small PVC pipe. The number of turns of the secondary is the ratio of the pipe diameter and the wire diameter. In this case, the wire diameter is 0.118 inches. So the number of turn on the secondary is approximately 102 turns. With the given dimension, the inductance value of the secondary can be calculated using the Wheeler formula,

$$L_2 = \frac{d^2 N^2}{18d+40l} \quad (20)$$

Where,

d is the diameter of the secondary coil

N is the number of turns on the secondary

l is the length of the secondary coil.

The capacitance of the secondary consisted of, 10, 2000pF capacitors in series. The capacitor used in the primary is a charging capacitor with the value of 0.235 μ F. Once L_2 is known, the primary inductance can be calculated:

$$L_1 = \frac{L_2 C_2}{C_1} \quad (21)$$

The parameters of the transformer are given in Table 6. The parasitic values were not characterized.

| COMPONENT | VALUE |
|-----------|-------|
|-----------|-------|

| | |
|-----------|----------------|
| C1 | 0.235 μ F |
| C2 | 200pF |
| L1 | 0.25 μ H |
| L2 | 250.09 μ H |
| $L_{1,s}$ | 0.3 μ H |
| $L_{1,o}$ | 0.4 μ H |

Table 6: Transformer Design Parameters

One last step was to determine the coupling coefficient. By using the RCL meter, the inductances of the primary when the circuit was opened ($L_{1,o} = 0.4\mu\text{H}$) was determined. Likewise, the inductance for the short circuit was determined ($L_{1,s} = 0.3\mu\text{H}$). The coupling coefficient then was calculated to be 0.5 according to this formula.

$$k = \sqrt{1 - \frac{L_{1,s}}{L_{1,o}}} \quad (22)$$

However, the RCL meter measured not only the pure inductances of the transformer wires but also the leads. This can create an increase (or uncertainty) in the primary inductance, which is the case for low inductance DRPTs. So the coupling coefficient is a variable that needed to be tweaked.

3.3 Multisim simulation

In this section, a Multisim model was used to predict the gain of the transformer. Figure 40 shows the completed Multisim model of the transformer. This model incorporated the transformer parameters. As mentioned earlier, the coupling coefficient was estimated for under coupled condition, so the simulation was done with various coupling coefficients ranging from 0.4-0.6. It is noted that the ideal number is 0.6.

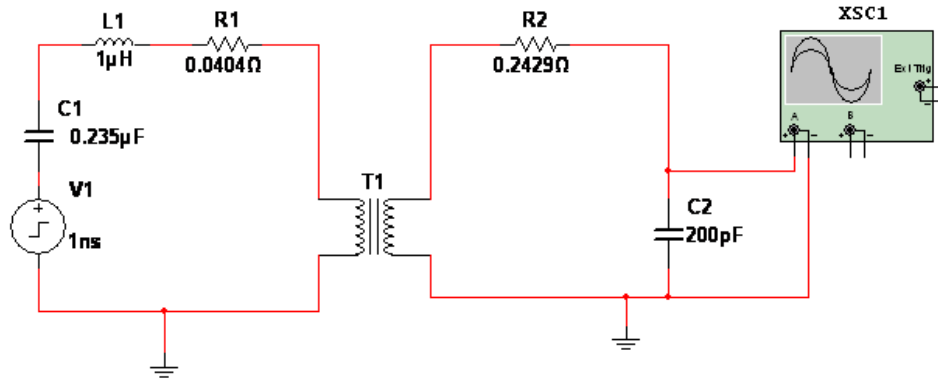


Figure 40: Multisim model of a helical transformer

In Figure 40, the voltage source is the square pulse source which has the rise/fall time of 1ns and the output of 1V. R1 and R2 represent the parasitic resistance of the windings. The C2 value is the secondary capacitance, which is the capacitor stack placed inside the secondary winding.

The inductances and the coupling coefficient of the transformer were specified in T1 (not shown in the figure), which are 0.25µH (for the primary inductance), 250.09µH (for the secondary inductance), and 0.4-0.6 (for the coupling coefficient). To determine the exact coupling coefficient, several simulations were made to compare with the experimental result, and the closest value will be the k factor of the transformer.

Table 7 is the summary of the simulations with various k factors.

| COUPLING COEFFICIENT(K) | SECONDARY VOLTAGE(GAIN) |
|-------------------------|-------------------------|
| 0.4 | 5.4 |
| 0.45 | 5.9 |
| 0.5 | 6.5 |
| 0.55 | 7.3 |
| 0.6 | 7.7 |

Table 7: Gain v.s. coupling coefficient of a helical transformer

Figure 41 shows the secondary voltage for k=0.6. It takes approximately 1.5 µs to reach the second peak, which is 1.333 times that of the first peak.

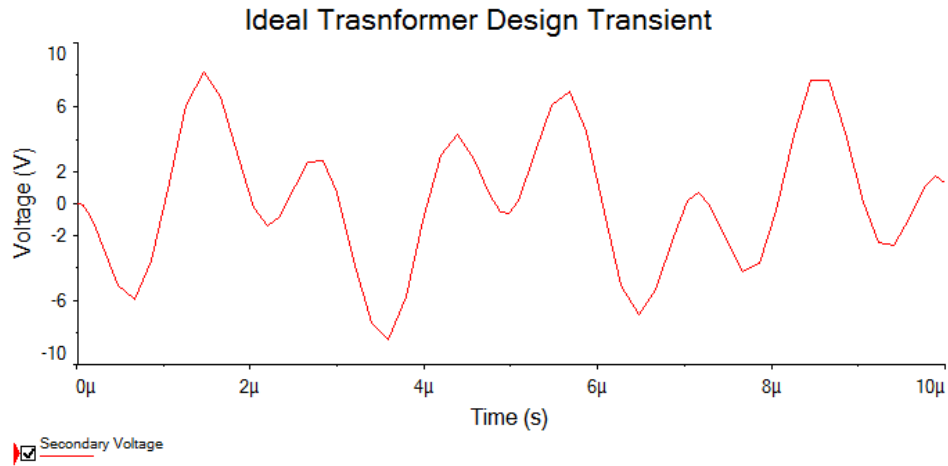


Figure 41: Transient of ideal coupling coefficient on a helical transformer

3.4 Experimental Setup

The transformer was tested for two different experimental configurations.

In both experiments, a spark gap switch was used for high voltage and high current ratings. We set the aim of producing the secondary voltage above 100 kV. In the first configuration, Figure 42 shows how the transformer was wired along with the spark gap, which is a manually-adjusted spark gap.

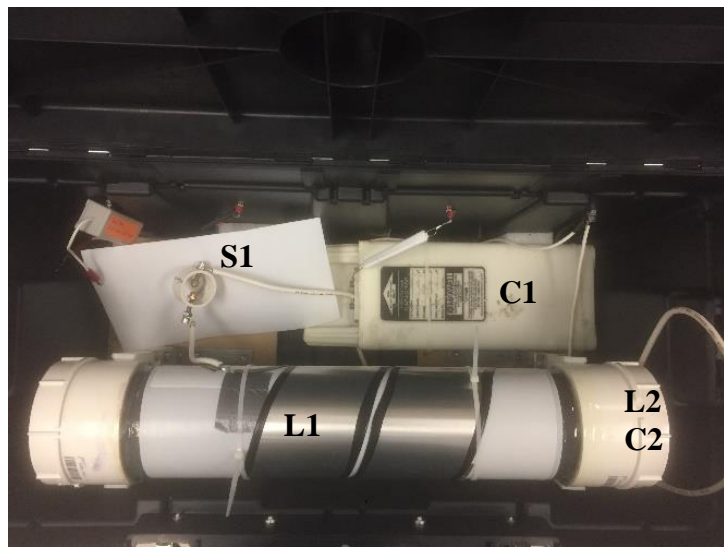
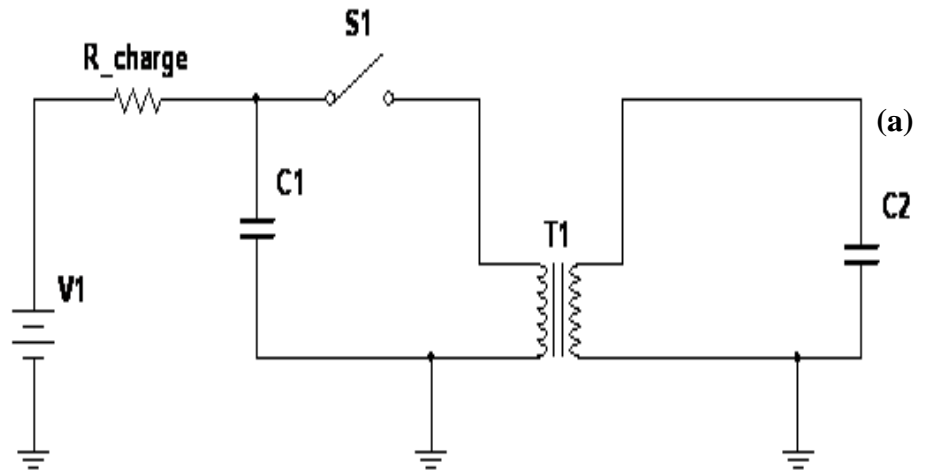


Figure 42: First experiment schematic and setup

In the second configuration, the transformer was connected with a trigatron, which allows pulses to be generated repeatedly without manually triggering. This system involves a three-terminal switch, which is wired similarly to a regular switch; however, the third terminal was connected to a controllable reed relay. A separate power supply was needed to power the reed relay circuit. The reed relay was controlled by a delay generator for various repetition rates. Figure 43 shows the experimental configuration.

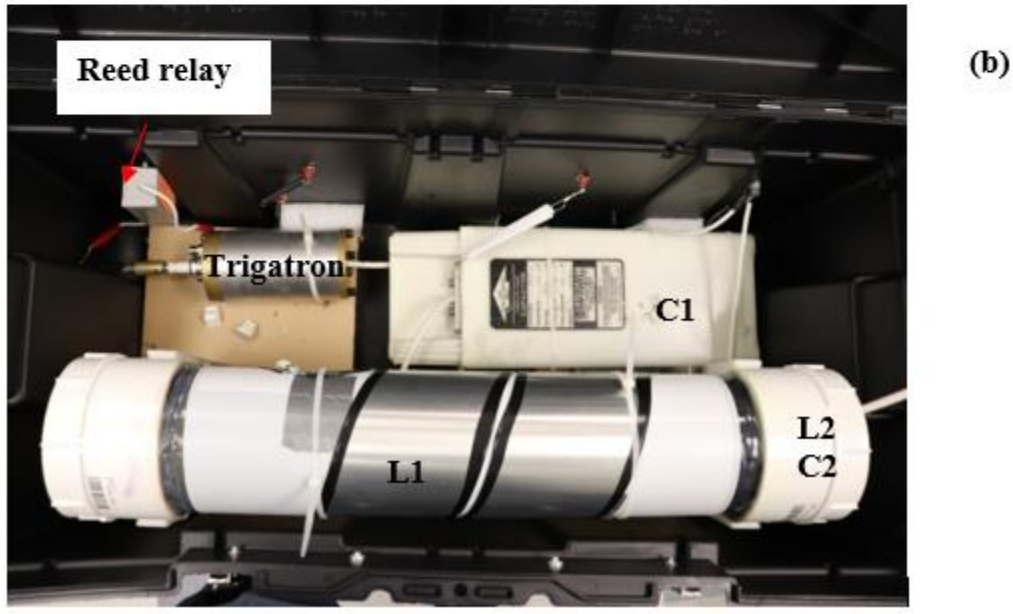
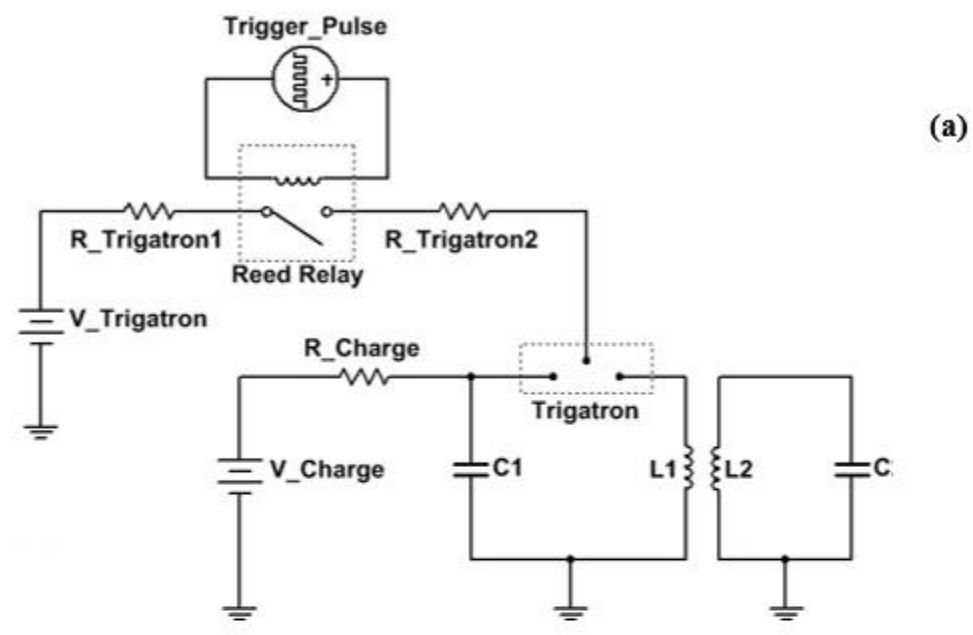


Figure 43: Second experiment schematic and setup

This experiment involved charging the reed relay and the primary capacitor at the same time. Once the relay is closed, the third terminal of the switch closes, which further closes the main switch, allowing the primary capacitor to discharge through the transformer.

3.5 Experimental Results

As mentioned earlier, the transformer gain was determined for various charging voltages. The experiment results were obtained by increasing the input voltages through adjusting the spark gap length. Table 8 shows the results.

| PRIMARY (INPUT VOLTAGE, KV) | SECONDARY (OUTPUT VOLTAGE, V) | SECONDARY X2(KV) | GAIN |
|-----------------------------|-------------------------------|------------------|----------|
| 2.78 | 11 | 22 | 7.913669 |
| 2.84 | 11.2 | 22.4 | 7.887324 |
| 3.12 | 11.4 | 22.8 | 7.307692 |
| 6.5 | 22.8 | 45.6 | 7.015385 |
| 6 | 22.8 | 45.6 | 7.6 |
| 6 | 22.6 | 45.2 | 7.533333 |
| 8.9 | 32.6 | 65.2 | 7.325843 |
| 9 | 32 | 64 | 7.111111 |
| 9.3 | 33.2 | 66.4 | 7.139785 |
| 13.7 | 46.8 | 93.6 | 6.832117 |
| 13.2 | 45.6 | 91.2 | 6.909091 |
| 13.6 | 45.6 | 91.2 | 6.705882 |
| 15.9 | 51.6 | 103.2 | 6.490566 |
| 15.3 | 51.4 | 102.8 | 6.718954 |
| 15.5 | 51.4 | 102.8 | 6.632258 |

Table 8: Measured secondary voltages for given primary voltages

The experiment results show a maximum output voltage was 102.8 kV for 15.5 kV input, which satisfies our goal. In the whole voltage range (2.78 kV to 15.5 kV), the gain is relatively constant from 7.9 to 6.6, which is quite linear (Figure 44).

According to the simulation, the coupling coefficient is related to the gain of the transformer, which allowed us to determine the coupling coefficient to be in the range of 0.5-0.55.

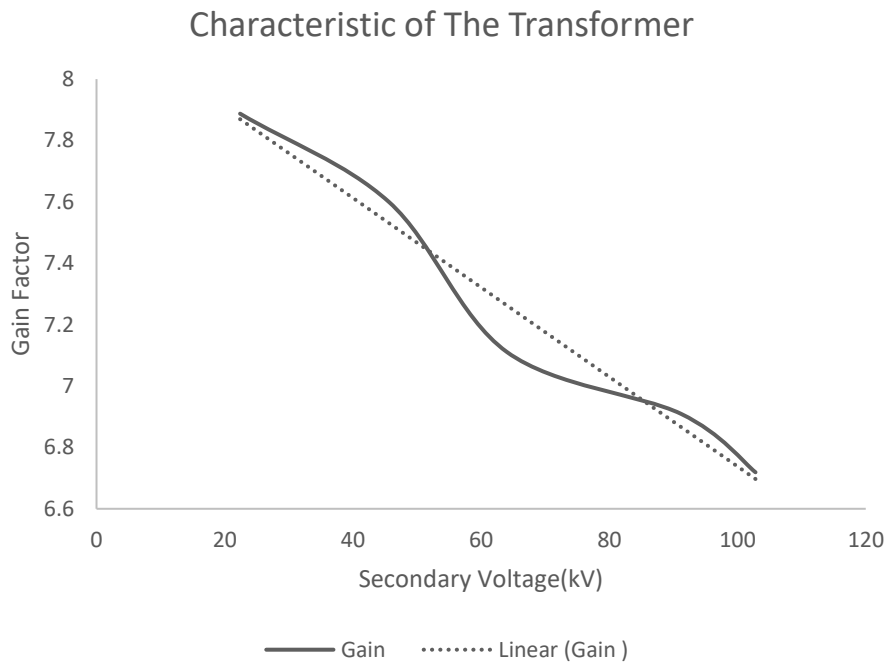


Figure 44: Transformer gain decay rate compares to linear trend line

In the next experimental configuration, the input voltage was set to 10kV. Then, the power supply of the reed relay was set to 7kV. Figure 45 shows the secondary voltage over time.

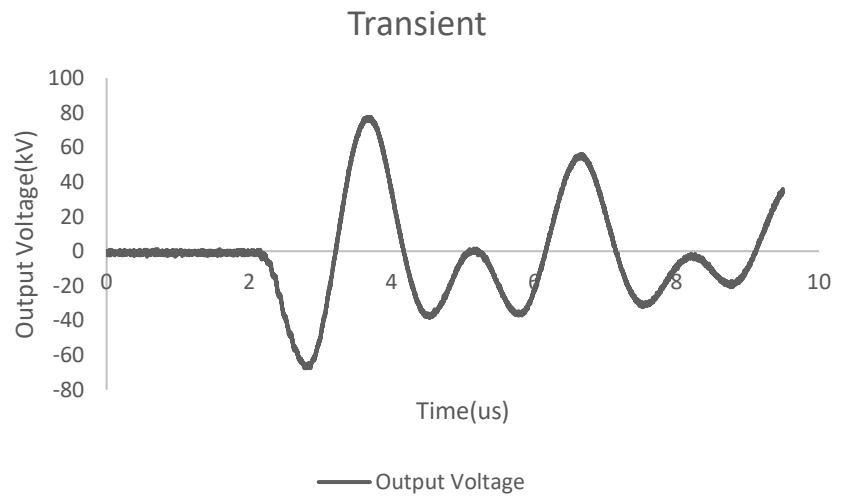


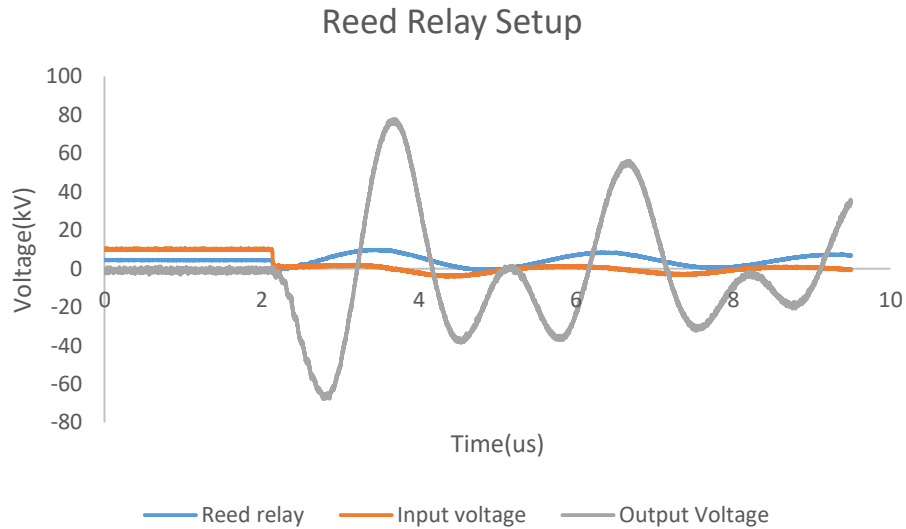
Figure 45: Helical transformer output transient**Figure 46: Reed relay triggered results along with input and output voltage of a helical transformer**

Figure 46 shows the readings from three channels of the oscilloscope. The blue line represents the reed relay. The orange line represents the input voltage. And, the grey line is the output voltage. At 2 μs, the reed relay was triggered. The input voltage of the transformer started to fall to zero. The output voltage takes 1.5 μs to reach its second peak.

3.6 Design 2: Toroidal Transformer

This section discusses the second type of transformer. It is a toroidal type and involves the dual resonant concept. This transformer has an ability of creating an ultrafast charging pulse on the order of hundreds of nanoseconds.

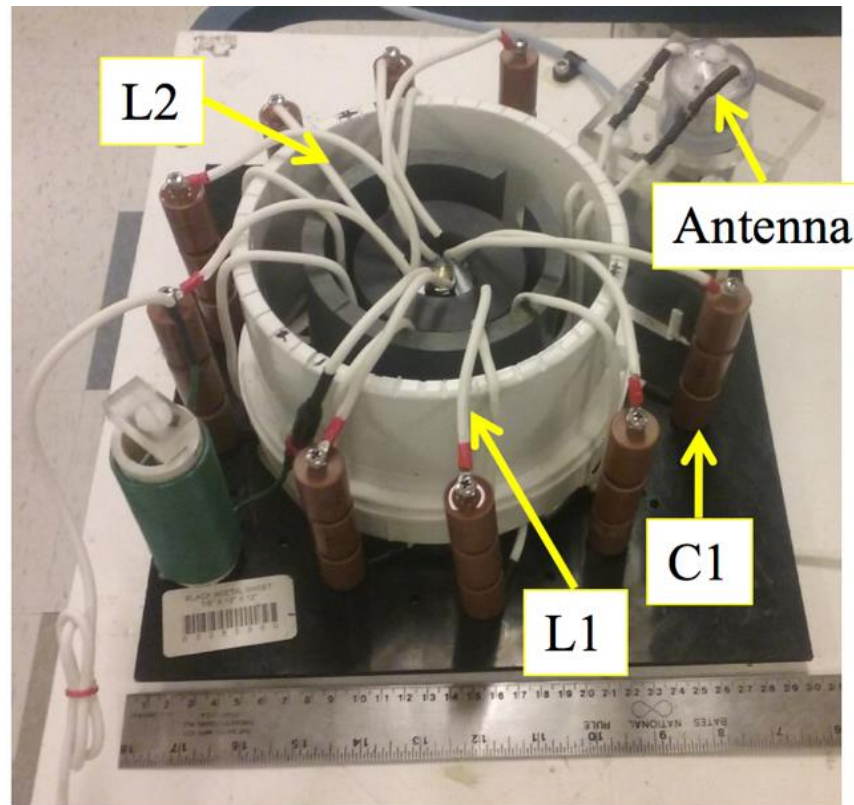


Figure 47: Toroidal DRPT design with label

In this design, the primary was made of nine capacitor stages in parallel which were connected to a transfer switch. Each capacitor stage has three capacitors connected in series. The primary inductance is the inherent inductance in the capacitor and the lead. The secondary winding was formed by seven turns of the high voltage cable. The cable was wound around the circular pipe.

The values of the transformers (Table 9) were plugged in the Multisim to simulate the output voltage (Figure 48).

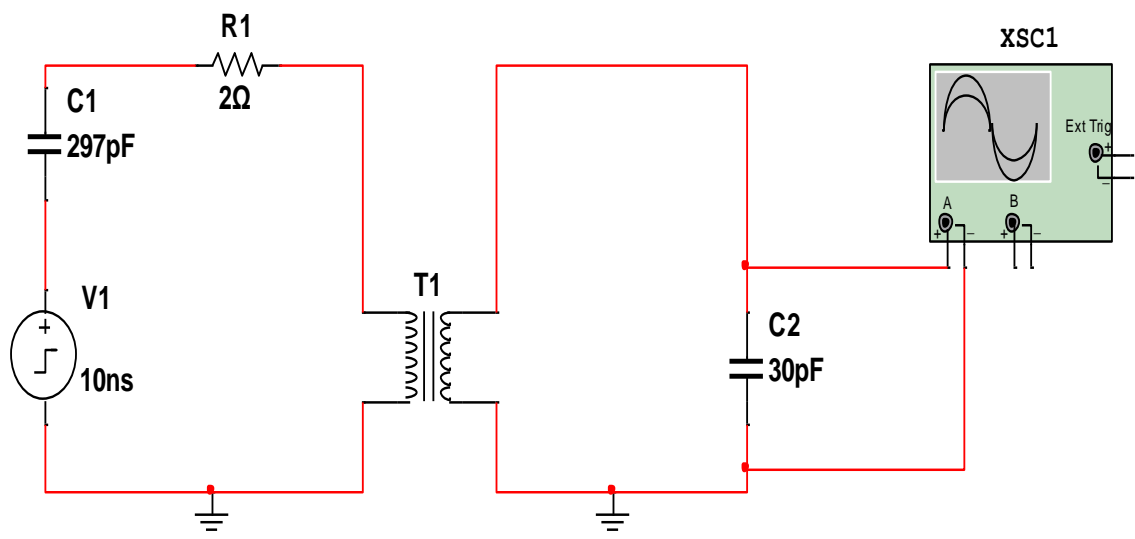


Figure 48: Toroidal DRPT simulation schematic

The simulation results show that the gain of the transformer is approximately 1.5.

| COMPONENT | VALUE |
|-----------|-------|
| L1 | 90nH |
| C1 | 297pF |
| L2 | 450nH |
| C2 | 30pF |

Table 9: Toroidal transformer values

Fig.50 shows the secondary voltage and the magnitude of the second peak represent the gain of the transformer. Very interestingly, although the gain is relatively low (only 1.5), this antenna is very fast and reaches its secondary peak in less than 30 ns.

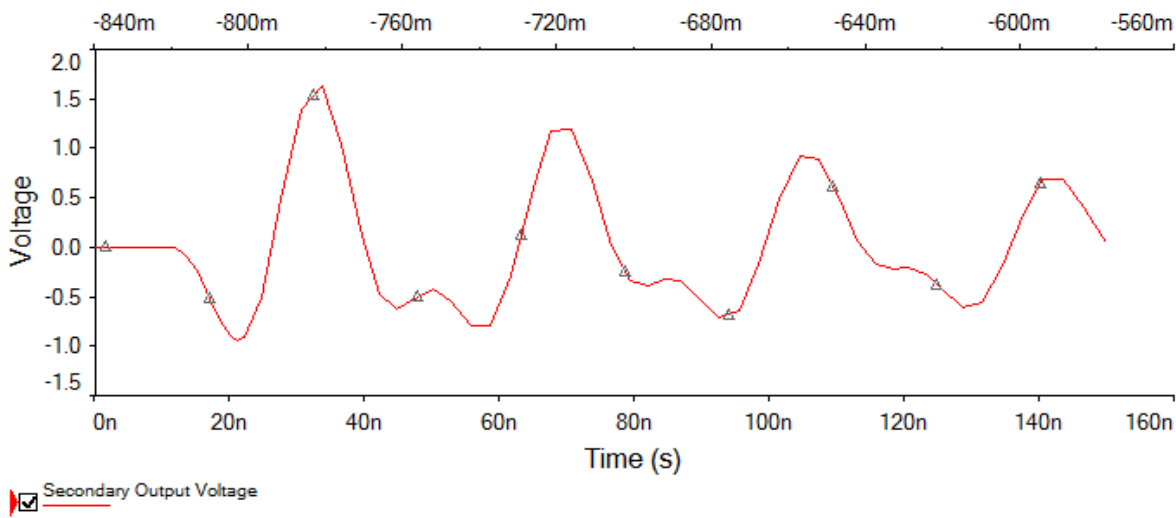


Figure 49: Simulated toroidal transformer result

Experimental results are shown in Figure 50. The gain is approximately 1, which is slightly lower than 1.5, the value simulated by Multisim. This transformer is however very fast and may be useful for breaking down a peaking switch at a high voltage (Figure 50b).

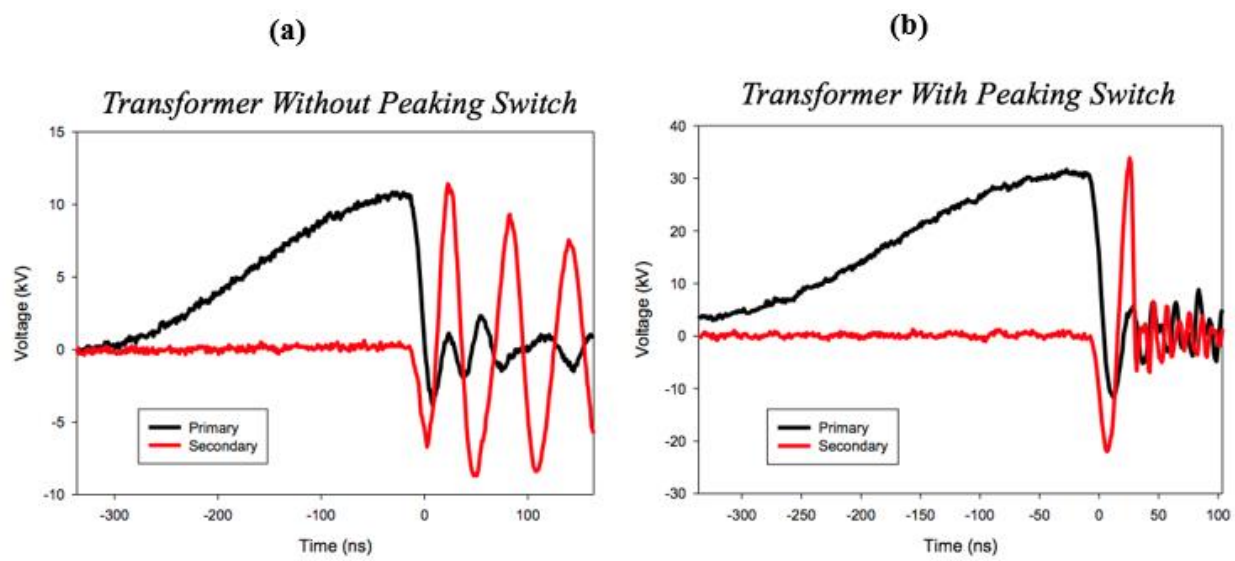


Figure 50: a) Toroidal DRPT output transient without peaking switch b) Toroidal DRPT output transient with peaking switch

3.7 Summary

Two types of transformers were designed: 1) high gain (6-7) and 2) low gain (1). The high gain transformer charges the load capacitor in 1.5 μ s, whereas the low gain transformer can do that in less than 100 ns. We found that the simulation results are comparable to the experimental results in both charging time and voltage gain, although the actual gain is typically smaller than the simulation value.

Chapter 4. Discussions

The dielectric biconical antenna produces the maximum electric field of 1.53 kV/cm, for an input voltage of 50kV. This is lower than that predicted from the low voltage input. At 1 kV input, the electric field was measured up to 0.12 kV/cm, which predicts the field to be 9.25 kV/cm for 50 kV input. In fact, the deviation of the linear trend takes place even at 30 kV. With this trend, the expected maximum electric field with this antenna might not produce the field higher than 2.5kV/cm, even with 100kV input voltage. The deviation of the linear relationship between output electric field and the input voltage is very likely caused by the dielectric failure, i.e., the dielectric constant of the material cannot sustain for high voltages. The antenna material is a compound material, but mostly zirconia. According to the datasheet of the dielectric material, the dielectric loss (or the tangent loss of material) ranges from 0.05-0.1. Any material that has tangent loss that is smaller than 0.01 is considered low-loss material. So, this material can be considered as lossy [43]. At high voltages, the dielectric loss may exacerbate, which however was not documented even by the manufacture.

A step to determine the behavior of this material is to use the network analyzer to identify the real and imaginary components of this dielectric material. In order to measure the dielectric properties of such material, a technique using an open ended coaxial probe can be considered. This method is simple and easy to extract the characteristic of the materials. To prepare for the measurement, a slice of measured sample should be prepared. In theory, the electric field travels along the coaxial cable freely until it reaches the terminus. As the inner conductor ends, energy flows into and deposits into the sample. The other energy gets reflected and the reflection coefficient can be measured, so the real and imaginary components of such material can be

extracted at sampled frequency. Thus, the tangent loss can be calculated [44-47]. This method however cannot predict the dielectric property at high voltages and thus has its limitations.

The helical transformer in Chapter 3 has an average gain of 7.3, which can produce 100kV with an input voltage of 15kV. The pulse width of the outputted waveform of the first transformer design is 1 microsecond, which agrees with the simulated result. On the other hand, the pulse width of the second transformer (a toroidal design) is in nanosecond range. The gain of both designs can be significantly increased by reducing the leakage flux at the primary side. The length of the primary winding introduces the leakage flux, which is an issue since the leakage inductance directly reduces the gain of the transformer. The issue was investigated by Multisim model. The model includes the parasitic inductances of the primary. By varying this value, the effects can be observed while measuring the output voltage.

| Parasitic Inductances Values | Transformer Gain |
|------------------------------|------------------|
| 1 μ H | 7.7 |
| 0.8 μ H | 10.3 |
| 0.6 μ H | 13.3 |
| 0.4 μ H | 17.7 |
| 0.2 μ H | 23.5 |

Table 10: A comparison of leakage inductances effects on transformer gain.

Table 10 shows the results of a series of simulation, which has various leakage inductance values on the primary side. The values start with the original design and a 20 percent decrement step. The recorded gain performs the best at 0.2 μ H, which is 80 percent smaller than the original design. The gain at 0.2 μ H shows the greatest magnitude with the output voltage of 23.5V for every 1V input. This high gain however is hard to implement because such small

inductance is too small to make as the winding has to be long enough to cover the PVC pipe. In theory, the amount of excessive wires that are needed to be removed has to match with 80 percent reduction on parasitic inductance value on the primary. It is quite challenging, a reduction of 40-60 percent of excess wires is more reasonable. This can improve the gain by approximately 2 times.

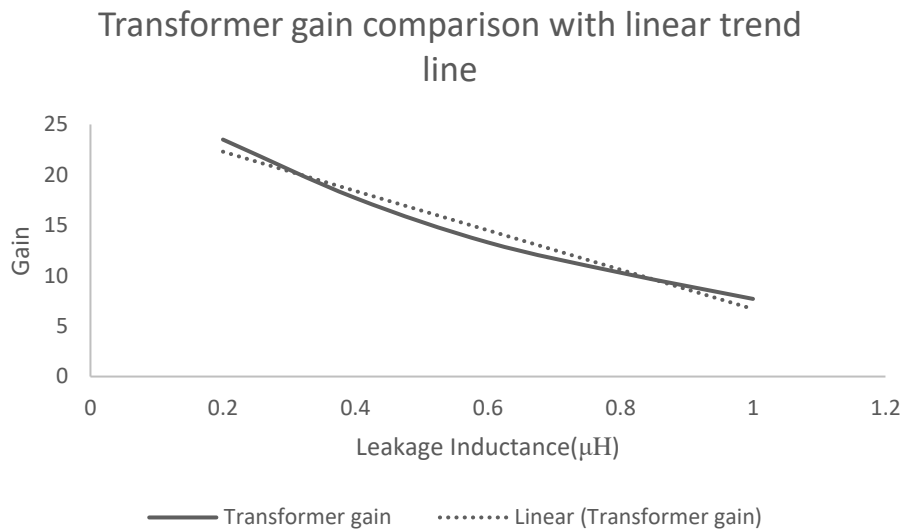


Figure 51: Decay rate of transformer as the leakage inductance increases compares to linear decay trend line

A following figure below shows the transients of these simulations. The most optimal transient should have the magnitude of the second peak is equal to two times the magnitude on the first peak. The transient of the ideal case, which has $0.2\mu\text{H}$ leakage inductances, shows the best characteristic.

Comparison of multiple leakage inductances and transformer gain

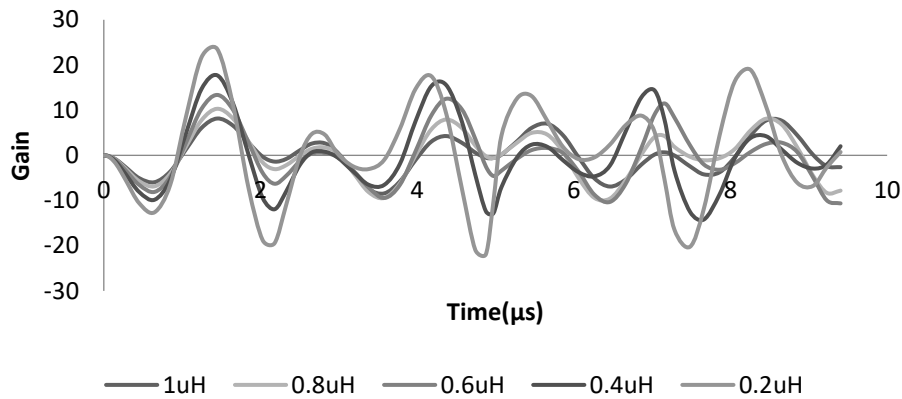


Figure 52: Transient of transformer with various leakage inductance values.

Future work

For future work, the tangent loss of this zirconia material has to be determined. A low-loss, low dispersion material should be used. This will improve the produced electric field intensity. A high dielectric constant material that has a tangent loss of 0.01 or smaller is preferable.

A spark gap switch, or transfer switch, is also needed to complete the EMP system. The integration of the transfer switch on the first transformer design will help to shorten the charging pulses from microsecond to nanosecond range. The parasitic values of the transformer are needed to be reduced by minimizing the amount of wires use to make interconnections.

Once the peaking switch and transfer switch are included, the system will be ready to use for testing the antenna.

Chapter 5. Summary

A dielectric biconical antenna (DiBiCA) was designed to target high dielectric material, for example skin. We showed that the antenna is capable of radiating an electric field of 1-1.5 kV/cm at a shallow depth of <1cm for a maximum voltage of 50 kV. Simulation results as well as experimental results agree to a large extent, although experimental results are generally lower. The antenna dielectric material exhibits a nonlinear trend and the efficiency deteriorates as voltage increases. This problem can only be resolved by a better dielectric material.

The DRPT has an average gain of approximately 7.3. This enables the transformer to produce over 100 kV with the input voltage of 15kV. To complete an EMP system, more work is needed to design the transfer switch and peaking switch. These switches will eventually allow the transformer pulse to be in the picosecond range. The toroidal transformer is an interesting option, as it may not need the transfer switch since the charging pulse is in less than 100 ns. But the peak switch is still needed. In general, the performance of the transformer can be predicted from the simulation.

REFERENCES

1. C. Baum, "From the electromagnetic pulse to high-power electromagnetics," Proceedings of the IEEE, vol. 80, no. 6, pp. 789–817, 1992
2. Petrella, R. A., K. H. Schoenbach, and S. Xiao. "A Dielectric Rod Antenna Driven by a Pulsed Power System." *IEEE Transactions on Dielectrics and Electrical Insulation* 24, no. 4 (2017): 2157–63. <https://doi.org/10.1109/TDEI.2017.006292>.
3. D. Higgins, K. Lee and L. Marin, "System-generated EMP", *IEEE Transactions on Antennas and Propagation*, vol. 26, no. 1, pp. 14-22, 1978.
4. Andreev, Yu. A., A. M. Efremov, V. I. Koshelev, B. M. Koval'chuk, V. V. Plisko, and K. N. Sukhushin. "Generation and Emission of High-Power Ultrabroadband Picosecond Pulses." *Journal of Communications Technology and Electronics* 56, no. 12 (December 2011): 1429–39. <https://doi.org/10.1134/S1064226911110027>.
5. Efremov, A. M., V. I. Koshelev, B. M. Kovalchuk, V. V. Plisko, and K. N. Sukhushin. "High-Power Sources of Ultra-Wideband Radiation with Subnanosecond Pulse Lengths." *Instruments and Experimental Techniques* 54, no. 1 (January 2011): 70–76. <https://doi.org/10.1134/S0020441211010052>.
6. Novac, B.M. & Sarkar, Preeti & Smith, Ivor & Banakhr, Fahd & Greenwood, C & Pecastaing, L & Ruscassie, R & Ferron, A & Pignolet, P. (2009). A novel and non-invasive pulsed electric field technique for industrial food processing. 1 - 4. 10.1049/cp.2009.1663.

7. "Transformer Construction of the Core and Transformer Design." Basic Electronics Tutorials (blog), August 31, 2013. <https://www.electronicstutorials.ws/transformer/transformer-construction.html>.
8. "1.1 Basic Transformer Theory." Accessed April 4, 2018. http://www.voltech.com/Articles/086-627/001/1_1_Basic_Transformer_Theory
9. Heathcote, Martin J., and D. P. Franklin. *The J & P Transformer Book: A Practical Technology of the Power Transformer*. 12th ed. Oxford ; Boston: Newnes, 1998.
10. P. Smith, *Transient Electronics*. New York, NY: John Wiley & Sons, 2002.
11. Xiao, Shu & Guo, Siqi & Nesin, Vasyl & Heller, Richard & H Schoenbach, Karl. (2011). Subnanosecond Electric Pulses Cause Membrane Permeabilization and Cell Death. *IEEE transactions on bio-medical engineering*. 58. 1239-45. 10.1109/TBME.2011.2112360.
12. Saidulu, V, K Srinivasa Rao, and P V D Somasekhar. "THE CHARACTERISTICS OF RECTANGULAR AND SQUARE PATCH ANTENNAS WITH SUPERSTRATE." *International Journal of Engineering Sciences* 6, no. 3 (n.d.): 10.
13. Valderas, Daniel, ed. *Ultrawideband Antennas: Design and Applications*. London: Imperial College Press, 2011.
14. [3]"Horn Antenna | Microwave Horn Pyramid / Corrugated | Radio-Electronics.Com", *Radio-electronics.com*, 2018. [Online]. Available: http://www.radio-electronics.com/info/antennas/horn_antenna/horn_antenna.php. [Accessed: 18- Apr- 2018].
15. Panzer, Ben. "DEVELOPMENT OF AN ELECTRICALLY SMALL VIVALDI ANTENNA: THE CReSIS AERIAL VIVALDI (CAV-A)," n.d., 82.

16. AN, YAKUP ERDO. "A THESIS SUBMITTED TO THE GRADUATE SCHOOL OF NATURAL AND APPLIED SCIENCES OF MIDDLE EAST TECHNICAL UNIVERSITY," n.d., 170.
17. Constantine A. Balanis. *Antenna theory - Analysis and design*. John Wiley and sons, 2005
18. J. F. Aurand [1997], "A TEM-Horn Antenna with Dielectric lens for Fast Impulse Response," in C. E. Baum et al (eds.), *Ultra-Wideband, Short-Pulse Electromagnetics 3*, new York, Plenum, pp. 113–120
19. Baum, Carl E., and Everett G. Farr. "Impulse Radiating Antennas." In *Ultra-Wideband, Short-Pulse Electromagnetics*, edited by Henry L. Bertoni, Lawrence Carin, and Leopold B. Felsen, 139–47. Boston, MA: Springer US, 1993. https://doi.org/10.1007/978-1-4615-2870-8_17.
20. C.E. Baum, E.G. Farr, and D.V. Giri, "Review of Impulse-Radiating Antennas", Ch. 16, pp. 403- 439, in W.R. Stone (ed.) *Review of Radio Science 1996-1999*, Oxford U. Press, 1999
21. C.E. Baum, "Variations on the Impulse-Radiating-Antenna Theme", *Sensor and Simulation Note 378*, February 1995
22. C. E. Baum and E. G. Farr, " Impulse Radiating Antennas," pp. 139-147 in H. L. Bertoni et al (eds.), *Ultra Wideband/Short-Pulse Electromagnetics*, Plenum Press, New York, 1993
23. C. E. Baum, L. Carin and A. P. Stone (eds.) *Ultra-Wideband, Short-Pulse Electromagnetics 3*, New York, Plenum, 1997

24. E. G. Farr, C. E. Baum and C. J. Buchenauer, Impulse Radiating Antennas, Part II, pp. 159-170 in L. Carin and L. B. Felsen (eds.) *Ultra-Wideband, Short-Pulse Electromagnetics*, New York, Plenum Press, 1995.
25. Rosenlind, J. (2009). The Impulse-Radiating Antenna. Master. Karlstads.
26. Kumar, Prashanth & E. Baum, Carl & Altunc, Serhat & Buchenauer, C & Xiao, Shu & Christodoulou, Christos & Schamiloglu, Edl & H. Schoenbach, Karl. (2011). A Hyperband Antenna to Launch and Focus Fast High-Voltage Pulses Onto Biological Targets. *Microwave Theory and Techniques, IEEE Transactions on*. 59. 1090 - 1101. 10.1109/TMTT.2011.2114110.
27. Farr, Everett & M. Atchley, Lanney & E. Ellibee, Donald & Altgilbers, Larry. (2018). A Solid Dielectric Lens Impulse Radiating Antenna Surrounded by a Cylindrical Shroud.
28. R. A. Petrella, K. H. Schoenbach and S. Xiao, "A Dielectric Rod Antenna for Picosecond Pulse Stimulation of Neurological Tissue," in *IEEE Transactions on Plasma Science*, vol. 44, no. 4, pp. 708-714, April 2016. doi: 10.1109/TPS.2016.2537213
29. G. Smith, "Teaching antenna radiation from a time-domain perspective", *American Journal of Physics*, vol. 69, no. 3, pp. 288-300, 2001.
30. Xu, Fern. "Use Coaxial Cable, Twisted Pair Cable or Fiber Optic Cable for LAN?," September 23, 2015. <https://www.linkedin.com/pulse/use-coaxial-cable-twisted-pair-fiber-optic-lan-fern-xu>.
31. "Ness Engineering Tech Data - Impedance Formulas." Accessed April 4, 2018. <http://www.nessengr.com/techdata/impedance/imped.html>.

32. Xiao, Shu & Semenov, Iurii & Petrella, Ross & Pakhomov, Andrei & H. Schoenbach, Karl. (2016). A subnanosecond electric pulse exposure system for biological cells. *Medical & Biological Engineering & Computing*. 55. 10.1007/s11517-016-1516-7.
33. Ross A. Petrella, Shu Xiao, "Characterization of a dielectric rod antenna used for radiating picosecond pulses", *Power Modulator and High Voltage Conference (IPMHVC) 2016 IEEE International*, pp. 426-429, 2016.
34. A. Petrella, Ross & Xiao, Shu & Katsuki, Sunao. (2016). An air core pulse transformer with a linearly integrated primary capacitor bank to achieve ultrafast charging. *IEEE Transactions on Dielectrics and Electrical Insulation*. 23. 2443-2449. 10.1109/TDEI.2016.7556524.
35. Lim, Soowon & Chuhyun, Cho & Hong-Je, Ryoo & Jong-Soo, Kim & Geun-Hie, Rim & Yun-Sik, Jin. (2011). Fabrication and Operation Testing of a Dual Resonance Pulse Transformer for PFL Pulse Charging. *Journal of Korean Physical Society*. 59. 3679-. 10.3938/jkps.59.3679.
36. "BBC - GCSE Bitesize: Transformers - Higher." Accessed April 4, 2018. http://www.bbc.co.uk/schools/gcsebitesize/science/add_ocr_pre_2011/electric_circuits/mainproducedrev5.shtml.
37. Venkata, S.s & Krishnamurthy, S. (2003). Transient electronics: pulsed circuit technology [Book Review]. *Power and Energy Magazine, IEEE*. 1. 64- 64. 10.1109/MPAE.2003.1192028.
38. C. Baum, W. Baker, W. Prather, J. Lehr, J. O'Loughlin, D. Giri, I. Smith, R. Altes, J. Fockler, D. McLemore, M. Abdalla and M. Skipper, "JOLT: a highly directive, very

- intensive, impulse-like radiator", *Proceedings of the IEEE*, vol. 92, no. 7, pp. 1096-1109, 2004.
39. Pecastaing, L & Rivaletto, M & Ferron, A & Pecquois, Romain & Vezinet, Rene & Diot, J.C. & Tortel, S. (2013). A 600KV resonant pulse transformer combined to a helical antenna. 10.1109/PPC.2013.6627619.
40. Rafael Mendes Duarte and Gordana Klaric Felic, "Analysis of the Coupling Coefficient in Inductive Energy Transfer Systems," *Active and Passive Electronic Components*, vol. 2014, Article ID 951624, 6 pages, 2014. doi:10.1155/2014/951624
41. Harold A. Wheeler, "Simple Inductance Formulas for Radio Coils," *Proceedings of the I.R.E.*, October 1928, pp. 1398-1400
42. *Eccosorb.eu*, 2018. [Online]. Available: <http://www.eccosorb.eu/sites/default/files/files/dielectric-chart.pdf>. [Accessed: 18- Apr- 2018].
43. *Basics of Measuring the Dielectric Properties of Materials*. Agilent Technologies. Santa Clara, Ca, 2014, pp. 1-34.
44. J. de los Santos , D. Garcia and J. A. Eiras, "Dielectric characterization of materials at microwave frequency range", *Materials Research*, vol. 6, pp. 97-101, 2002.
45. T. P. Marsland and S. Evans, "Dielectric measurements with an open-ended coaxial probe," in *IEE Proceedings H - Microwaves, Antennas and Propagation*, vol. 134, no. 4, pp. 341-349, August 1987.
46. S. S. Stuchly, M. A. Rzepecka and M. F. Iskander, "Permittivity Measurements at Microwave Frequencies Using Lumped Elements," in *IEEE Transactions on Instrumentation and Measurement*, vol. 23, no. 1, pp. 56-62, March 1974.

47. *IPC-TM-650 Test Methods Manual*. No. 2.5.5.10, IPC, Bannockburn, IL, 2005, pp. 1-8.
48. García, D.; Eiras, J.A. *Ferroelectrics*, v. 123, p. 51-59,1991.
49. Sarkar, P., B. M. Novac, I. R. Smith, and R. A. Miller. "A High-Repetition Rate Closing Switch for EMP Applications," 97–100. IEEE, 2007.
<https://doi.org/10.1109/PPPS.2007.4651798>.
50. Duvillaret, Lionel & RIALLAND, Stéphane & COUTAZ, Jean-Louis. (2002). Electro-optic sensors for electric field measurements. I. Theoretical comparison among different modulation techniques. *Journal of the Optical Society of America B*. 19. 2692-2703.
10.1364/JOSAB.19.002692
51. G. Bustos, "SKYPE PRESENTATION of eoSense INSTRUMENT", 2018.
52. Kölbl, J, M Fröschl, A Seedsman, Y Gao, and M Dawson. "Fast Switching Pockels Cell Driver for SLR Laser System," n.d., 6.
53. R. Goldstein, 2018. [Online]. Available: <http://www.fastpulse.com/pdf/pcp.pdf>.
[Accessed: 18- Apr- 2018].
54. Goldstein, Robert. (1986). *ELECTRO-OPTIC DEVICES IN REVIEW*.. 5. 67-73.
55. C. Zhu, "Dielectric loss", National University of Singapore, 2018.
56. G. Awuah, H. Ramaswamy and J. Tang, Radio frequency heating in food processing.

APPENDICES

APPENDIX A- Peaking switch

A spark-gap switch can be turned on very rapidly, which can convert a slow rise time pulse to a fast rise time pulse. Such switch is a peaking switch. Peaking switches are usually filled with high pressure gas or liquid. Oil peaking switch is a good option as it is relatively simple, low cost, and easy to construct. [48,49]

A peaking switch is usually integrated in a parallel plate transmission line, which can guide the pulse transient to the load, which in an EMP system is a high power, wideband antenna. The parallel plate transmission line design is a crucial part since it will provide a balanced waveguide as the fast transient gets off the spark gap. (Figure 53) The desired gap distance of the peaking switch is related to the breakdown voltage and breakdown time it takes for the output voltage to reach its maximum. In this application, the desired maximum magnitude is at the second peak of the charging pulse. The high voltage transient is delivered to the antenna for radiation. [6, 49]

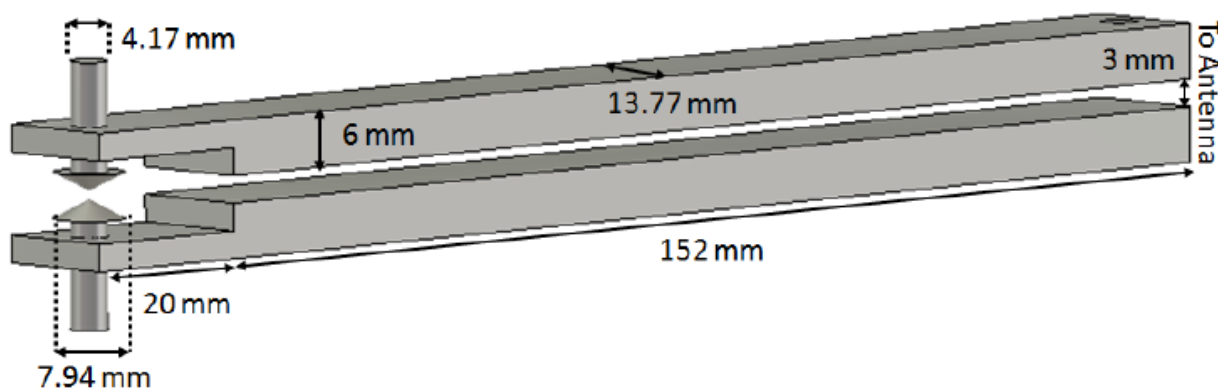


Figure 53: Peaking switch with parallel plate transmission line integration

APPENDIX B - Optic probe

An electro optic probe is used to measure electric fields without electrically disturbing the fields. The antenna measurements in this thesis were performed using an optic probe, eoProbes (Kapteos, France).

The probe is based on the electro-optic effect in which the refractive index of a fiber changes linearly with the applied electric field (the Pockels' effect).

The Pockels' cell contains voltage-controlled wave plates, which are also used to rotate the polarization of a beam passing through. A combination of Pockels cells with polarizers allows the conversion of the electric field to the phase changes [50-55] (See Figure 54).

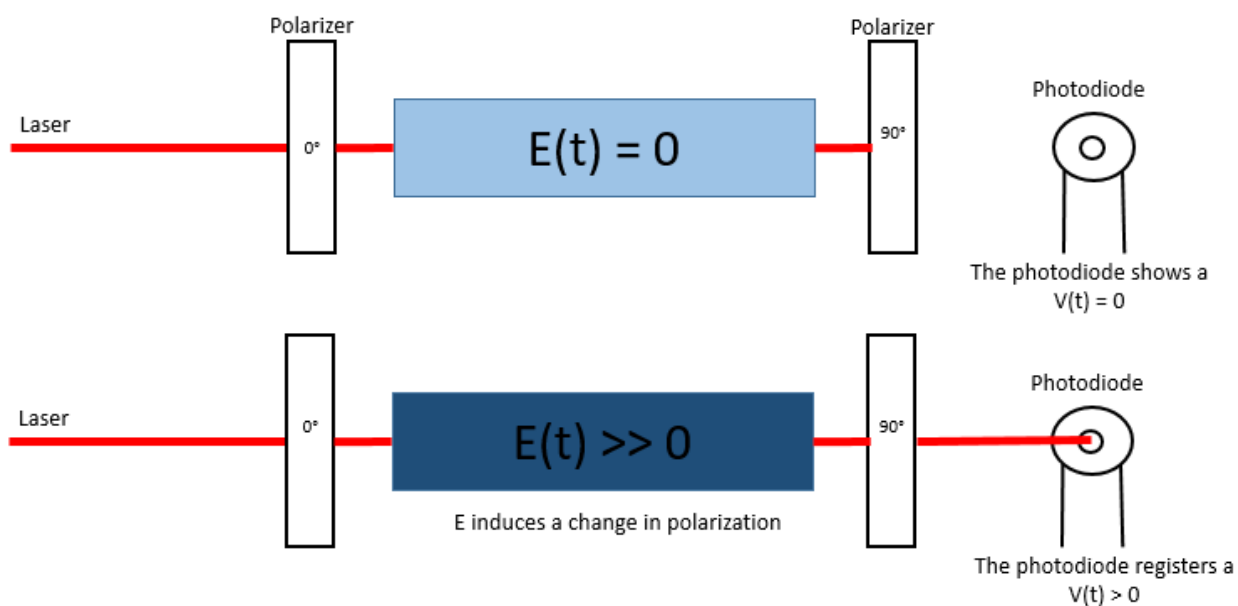


Figure 54: A combination Pockels cells with polarizer for Electric field sensing

The changes are read out by a data acquisition system in the eoSense instrument, then the eoSense software analyzes them and display the probe factor (AF). The final electric field is calculated by multiplying the measured electric fields with the probe factor. Figure 55 shows the setup of this optic probe. [52]

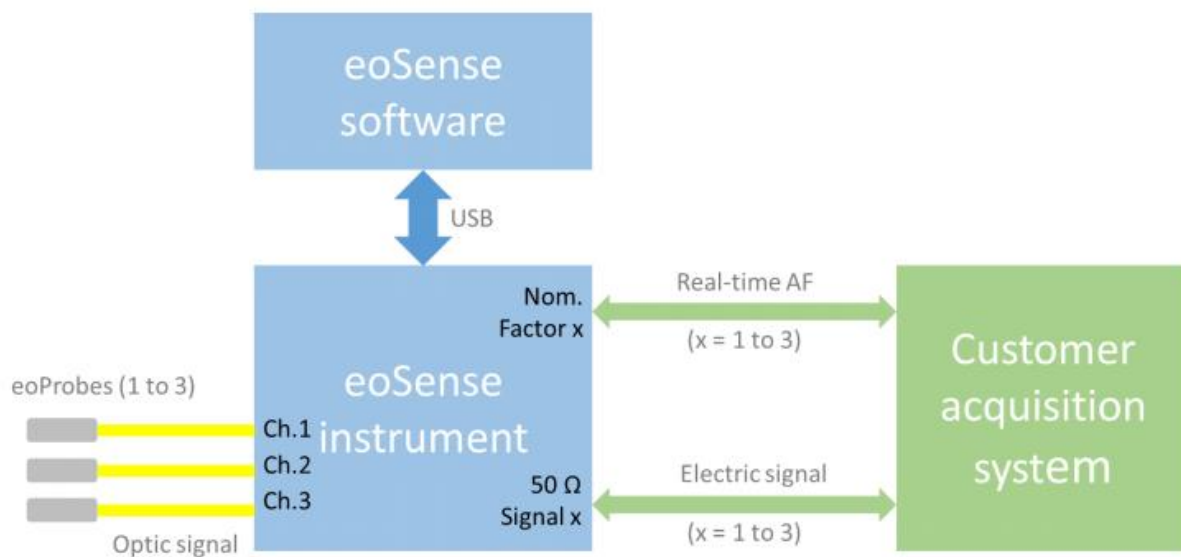


Figure 55: eoProbes setup for electric field measurements.

APPENDIX C - Dielectric loss

A low-loss dielectric material has limited dissipation of energy once a varying charge is applied. There are two main forms of losses in dielectric, conduction loss and dielectric loss. In general, conduction loss means energy dissipation through resistive current through the material. On the other hand, dielectric loss is the dissipation of energy base on the movement of charge in alternating electromagnetic fields through displacement current. [55-56]

Typically, a dielectric constant ϵ_r is a complex number, which can be expressed as

$$\epsilon_r = \epsilon_r' - j\epsilon_r'' \quad (24)$$

Where,

ϵ_r' is real component

ϵ_r'' is imaginary component

The real component represents the static dielectric contribution of the capacitance, whereas the imaginary part represents the energy loss in dielectric material [55-56]. And, the loss tangent is the ratio of the imaginary component to the real component.

$$\frac{\epsilon_r''}{\epsilon_r'} = \tan \delta \quad (25)$$

Another way to express dielectric loss material is its attenuation factor and penetration depth. In dielectric material, the intensity of the electric field decreases as it travels within the dielectric material. For example, the electric field travels from the surface into the dielectric material, the magnitude of the electric field will be decreased by a factor of

$$E = E_o e^{-\alpha x} \quad (26)$$

Where, α is the attenuation factor, x is the direction of the electric field. The attenuation factor mainly depends on the properties of the dielectric materials, which can be expressed as: [56-57]

$$\alpha = \frac{2\pi}{\lambda_0} \left[\frac{\varepsilon_r' \left(\sqrt{1 + \left(\frac{\varepsilon_r''}{\varepsilon_r'} \right)^2} - 1 \right)}{2} \right]^{\frac{1}{2}} \quad (27)$$

The penetration depth is defined as the input field decreases to $\frac{1}{e}$, where e is equaled to 2.718. With given dielectric properties, the penetration depth is inversely proportional to a specific frequency. This represents the ability to guide the electromagnetic waves in a dielectric material. The penetration depth of a lossy material can be calculation using [55-56]

$$d_p = \frac{c}{2\pi f \sqrt{2\varepsilon_r' [\sqrt{1 + (\tan \delta)^2} - 1]}} \quad (28)$$

VITA

Khiem Huynh received his B.S degree in Electrical Engineering from Old Dominion University, US, in 2016.